

# An Automatic Detection Algorithm for Sea Breeze Fronts: A Case Study over the Gulf of Guinea in West Africa

Thomas D'Aquin Allagbe<sup>1,2\*</sup>, François K. Guedje<sup>1,2</sup>, Houeto V. V. Arnaud<sup>1</sup>,  
Gandomè Mayeul Léger Davy Quenum<sup>2</sup>

<sup>1</sup>Laboratoire de Physique de l'Atmosphère (LPA), University of Abomey-Calavi, Abomey-Calavi, Benin

<sup>2</sup>International Chair in Mathematical Physics and Applications (ICMPA), University of Abomey-Calavi, Abomey-Calavi, Benin

Email: \*thomasdaquin.allagbe@uac.bj

**How to cite this paper:** Allagbe, T.D., Guedje, F.K., Arnaud, H.V.V. and Quenum, G.M.L.D. (2025) An Automatic Detection Algorithm for Sea Breeze Fronts: A Case Study over the Gulf of Guinea in West Africa. *Atmospheric and Climate Sciences*, 15, 330-361.

<https://doi.org/10.4236/acs.2025.152017>

**Received:** January 19, 2025

**Accepted:** March 21, 2025

**Published:** March 24, 2025

Copyright © 2025 by author(s) and Scientific Research Publishing Inc. This work is licensed under the Creative Commons Attribution International License (CC BY 4.0).

<http://creativecommons.org/licenses/by/4.0/>



Open Access

## Abstract

In this paper, we present a new approach to the detection of Sea Breeze Fronts (SBF) in the Gulf of Guinea using automated methods. The study focuses on southern West Africa, where SBFs play a crucial role in local weather. The research demonstrates that the dynamic of SBFs exerts a significant influence on local weather conditions and acts as a favourable mechanism for convection. The aim of this study is to improve the effectiveness of conventional SBF detection techniques by applying an automated methodology through the analysis of images obtained by the second generation Meteosat (MSG) satellite. Our method, based on an active contour technique called morphological snake, is capable of automatically detecting the cumulus lines that are associated with SBF in a relatively short period of time using a substantial number of MSG images taken every 15 min. To delineate the SBFs and to model their inland propagation by isochrones, several regression methods were employed. Among these, the kernel-weighted local polynomial regression (kwLPR) provided the greatest accuracy in modeling the SBF propagation, with an average spatial root mean square error (RMSE) of only 0.0034°. The SBF penetrated as far as 100 to 146.3 km inland at certain longitudes. Its average penetration along the coast is 103.17 km. The algorithm is highly robust and has a wide range of practical applications, including automatic pattern recognition and dynamic imaging. Furthermore, it has significant potential for future research into other complex phenomena, such as the propagation of pollutants and other atmospheric particles.

## Keywords

Sea Breeze Front, Automatic Detection, Morphological Snake, Meteosat, Gulf of Guinea, West Africa

## 1. Introduction

Due to the thermal contrast as a consequence of different heat capacities between ocean and land, coastal regions are favorable areas for the occurrence of land-sea breeze (LSB) circulations [1] [2]. As the land-sea thermal contrast increases during daytime, a pressure gradient occurs in the lower atmosphere, triggering Sea Breeze (SB) near the land surface. The SB circulation (SBC) is a vertically rotating mesoscale cell, with a shoreward flow near the land surface, upward air currents inland, downward currents that spread several kilometers out to sea, and (generally) a return flow to sea near 900 hPa [3]. Detailed descriptions and reviews of earlier works on LSB circulations are documented in [4]-[6]. Simpson *et al.* (1995) analyzed the classic sea breeze, its variations, and the mechanisms of the breeze front, examining their effects on air quality using observational techniques and physical and mathematical models. Planchon *et al.* (1997) explored the impact of sea breezes on precipitation through numerical simulations using a three-dimensional mesoscale model. The limit of penetration of this SB inland is called the sea breeze front (SBF). The SBF is the landward of the leading edge of the SBC, often associated with sudden changes in temperature, humidity and wind. Its approach can be marked by the development of fair-weather cumulus clouds (Cu). The spatial organization of this cloud line and its progressive movement make it possible to locate the SBF and calculate its penetration inland. The cool onshore breeze during the day, when air is rising over the heated land surface, has a direct influence on the formation of convective clouds and thus, the weather conditions such as daytime temperature, humidity and precipitation. These systems can also relieve oppressive hot weather, trigger thunderstorms, provide moisture for fog and improve or reduce air quality near the land surface. The SB circulation plays a key role in coastal regions, not only in convection and precipitation, but also in air quality, which affects the health of the coastal population [7]-[9]. SB circulation also plays an important role in urban pollution management, as shown by studies in areas such as Boston, where SB circulation affects the distribution of pollutants such as NO<sub>2</sub> and O<sub>3</sub> [10]. By influencing air quality, these breezes have an indirect impact on public health and urban planning efforts [10]. While these phenomena have been studied extensively in regions such as Boston, their role in fast-growing areas such as West Africa deserves special attention, especially in light of the growing challenges associated with rapid urbanisation and the effects of climate change. In addition to their influence on air quality, SBs play a crucial role in atmospheric dynamics, as illustrated by the ESCAPE (Experiment of SB Convection, Aerosols, Precipitation, and Environment) initiative. Funded by the National Science Foundation, this program has carried out in-depth studies of the interactions between SBs, aerosols and meteorological systems, in order to better understand and predict the formation of convective clouds and precipitation, particularly in tropical and subtropical environments [11]. [12] [13] showed that convection associated with the SBF acts as a favorable mechanism for triggering convection and inducing precipitation over coastal and inland areas. At present, there are almost no

studies of convection induced by sea breeze and land breeze fronts (SBF/LBF) during extreme events in West Africa. It is therefore of the utmost importance to improve our knowledge of SBF/LBF characteristics in the densely populated Guinean coastal region of West Africa. Therefore, it is of utmost importance to improve our knowledge of SBF/LBF characteristics over the densely populated Guinean coastal region of West Africa.

In tropical climates with seasonal alternation of the rainy and dry seasons, the dry season is the most favorable to the development of the SB circulation (e.g., Guedje-*et al.* 2019) because of the strong insolation and thus strong heating of land masses [14]. In addition, in these tropical areas, the Gulf of Guinea region offers a flat coastal plain that allows the SB to penetrate far inland. In some regions (Sergipe in Brazil, for example), the front resulting from this inland breeze extends over the continent by up to 100 km [15]. The extent of inland sea breeze penetration (or the horizontal scale of the sea breeze circulation cell) in mid-latitude regions is less than 100 km in some areas [16] and up to 500 km in others as in the case of northern Australia [17]. In addition to its inland extension, several other characteristics (location, rotation, initiation and cessation) based on observations have been examined by [18] [19]. Moisseeva and Steyn [20] also examined the diurnal evolution of SB rotation over an island in Sardinia, using observation-based hodographs. The dynamics of the SBF and its inland penetration have also been studied by Simpson *et al.* [21], who used the Froude number to simulate certain characteristics (deceleration around midday and acceleration later in the day) and frontogenesis by Miller *et al.* [3] as an increase in the amplitude of the translittoral potential temperature gradient with different factors controlling its inland penetration. To map and predict SBFs in southern Australia, Simpson *et al.* [21] used radar, lidar and satellite images in their studies. The updrafts of the SBF can lead to cloud formation, induce convection and influence the diffusion of pollutants and insects [22] [23]. Rainfall associated with mesoscale convective systems is a priority concern for researchers and scientists, with the aim of reducing vulnerability to hydrometeorological risks and improving early warning systems [24]-[26]. In West Africa, the rainy season can begin several weeks before the first rains, and the early rainfall during the rainy season can have a strong influence on local hydrological processes [27] [28]. Among the factors influencing these processes, where temperature sensitive SBs dominate, and where rapidly urbanizing populations are vulnerable to the risk of flooding, deforestation appears to be one effective way of triggering storms near the coast [29]. In addition, the southern part of West Africa (a region dependent on rain-fed agriculture and vulnerable to droughts and floods) has experienced significant deforestation since the 1950s [30]. In areas of coastal deforestation (e.g., Côte d'Ivoire), increased winds lead to convection of SBs inland, resulting in reduced evening rainfall over deforested areas [30]. In order to make a meaningful contribution to the existing body of knowledge, the present study focuses on the determination of SBF, which is a particularly important phenomenon in coastal areas such as the West African mon-

soon. According to Maranan *et al.* [31], sea breezes and overland convection favour isolated warm precipitation (ISE), particularly in the humid southern zones of West Africa.

Satellite images, particularly in the visible spectrum, are crucial for monitoring convective clouds and precipitation associated with SBFs, providing a better understanding of their dynamics and spatio-temporal variations. In this channel, visible light is efficiently reflected by the clouds, making them very bright and distinct in the visible images. On the other hand, in infrared images, the distinction between thin clouds and other atmospheric structures may be less marked, particularly if the temperature of these clouds is close to that of the ambient environment. Visible Meteosat images were used by Cautenet *et al.* [26] to validate numerical simulations during the dry season, while [32] highlighted their advantage in detecting clouds and contours, despite problems such as ground heat reflection which sometimes complicates infrared detection. Meteosat infrared thermal data and field measurements were used by Lensky *et al.* [33] to characterize the SBC under clear summer skies and assess the impacts of synoptic circulation. Several authors [15] [32] [34] [35] have used visible satellite imagery, with methods ranging from manual geographic information systems (GIS) approaches combined with in-situ observations to automated computer vision techniques.

Although conventional methods are capable of highlighting certain limits, these techniques still suffer from a lack of precision and the design of approaches based on limits (edges) is of paramount importance [36]. Existing popular techniques can be classified into two families: a) local techniques such as edge detectors which use image filtering and local information and b) active edge techniques such as “snakes” or “balloons” based on information along boundaries [37] [38]. Corpetti *et al.* [35] developed a method for detecting SBFs on Meteosat images based on wavelet coefficients using generalised Gaussian density (GGD). However, calculations based on GGD are very time-consuming. In addition, the method was not tested—with a wide data time series. The same methods from the computer vision community were recently adopted by Ferdiansyah *et al.* [34] [39], who applied a morphological snake algorithm (active contour method) for the detection of SBF clouds in Himawari-8 visible band images. Subsequently, they performed a manual selection of days with SB on the basis of observations made prior to the detection of contours by morphological applications. Similarly, Papolu *et al.* [40] implemented an SBF detection framework based on the morphological snake algorithm using a growing region approach with an area threshold set at 3500 pixel units. Corpetti *et al.* [35] previously demonstrated that this approach had limitations when applied to MSG images. However, their method allowed the implementation of a graphical user interface. In order to address these shortcomings and improve existing classical methods, we implemented an automatic snake algorithm applied to MSG images for the first time in the Gulf of Guinea.

We used an automatic method based on active contours (morphological snake algorithm) to identify SBFs, a robust approach applied for the first time to MSG

satellite images in the Gulf of Guinea, in order to study these characteristics. This work uses this method to analyse the characteristics of SBFs by exploring some dynamic aspects of particular cases and to initiate a climatology of their occurrence from February 2013 to 2018 (the last dry month before the first rainy season) in the Gulf of Guinea (this period covers the operational period of METEOSAT-10). Section 2 details the study area, data and methods, Section 3 presents the results and discussions, and Section 4 concludes with an outlook.

## 2. Study Area, Data and Methods

### 2.1. Study Area

The study focuses on the West African coastline along the Gulf of Guinea, which ranges from 2°S to 10°N and 8°W to 10°E. The seasonal cycle of rainfall in the Guinea Coast region is characterized by distinct dry and rainy seasons, subdivided into the main dry season from December to February (DJF), the start of the main rainy season in March-April, the main rainy season in May-June, the minor dry season from end of June to September (JAS) and the minor rainy season in October according to Guedje *et al.* [41]. This area has a relatively flat topography (**Figure 1**) with coastal plains that favor the penetration of the SB.

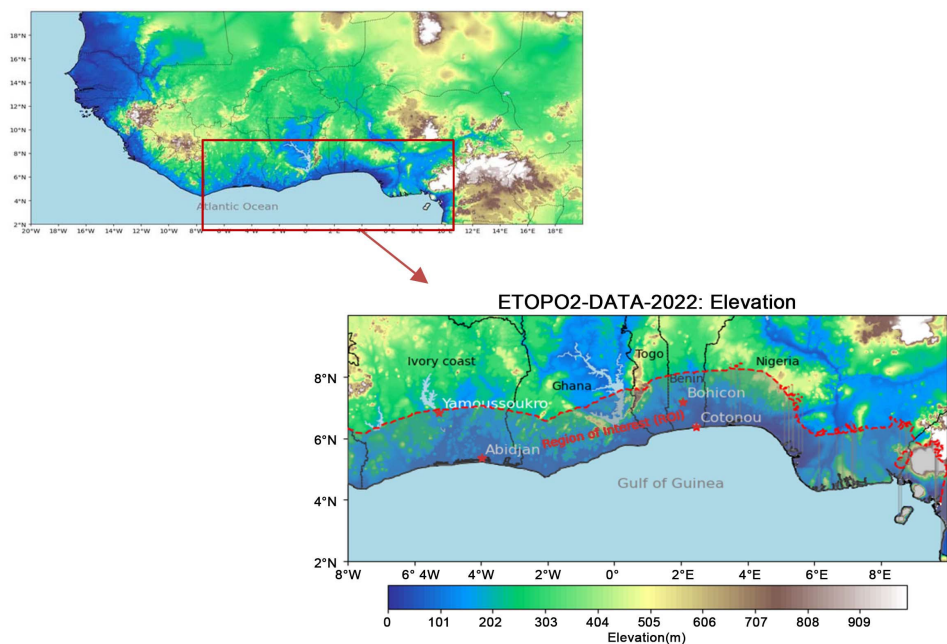


**Figure 1.** Topography of the study area. ETOPO2 (Earth TOPOgraphy data version 2) is a transparent, full-coverage topographic, bathymetric and bare-earth elevation dataset used in coastal hazard modeling. It is generated from digital seabed and land elevation databases on a 2-minute latitude/longitude grid [42]. Coloured areas indicate topography (in meters of elevation), coastal countries are named in black and stations in red stars. The dotted red line delimiting the Region of Interest (ROI) in shadow is the interpolated coastline at a distance of 1.8° (longitude/latitude). Elevation data are provided by the National Centers for Environmental Information website <https://www.ncei.noaa.gov/products/etopo-global-relief-model> of the National Oceanic and Atmospheric Administration (NOAA).

## 2.2. Satellite Data

Satellite imagery, with its high temporal, spectral and spatial resolution, such as SEVIRI on the MSG satellites (multispectral with a resolution of 3 km at nadir, HRV of 1 km) transmits images every 15 minutes and enables regular, high-resolution detection of localised phenomena such as convective clouds and thunderstorms, thus surpassing in-situ observations [43]. (See **Table 1**)

**Table 1.** Spectral, spatial and temporal characteristics of SEVIRI channels relevant in this study.

Channel name	Spectral band	Spatial resolution	Pixels pl
Visible (VIS0.8)	0.74 - 0.88 ( $\mu\text{m}$ )	3 km	3712
Visible (HRV)	0.5 - 0.9 ( $\mu\text{m}$ )	1 km	5568
Temporal resolution	15 minutes		

The data can be accessed via the EUMETSAT Earth Observation Portal at <https://eoportal.eumetsat.int/>. We use MSG greyscale images (JPG format) for the DJF 2013-2018 period, which is favourable to SB development, applying morphological transformations to them for analysis. To illustrate the synoptic weather conditions during the case studies used to demonstrate the capability of the algorithm we exploited ERA5 data for two days (12 January 2017 and 7 February 2018). The cases of convection linked to the SB during these days are studied for their presence of well-developed cumulus clouds and favourable observation conditions with Meteosat.

## 2.3. Methodology

On satellite images, the SBF is generally detected inland by an alignment of cumulus clouds approximately parallel to the coast. However, not all SBF episodes are easily visible, for example, when humidity is low, or may be masked on satellite images by larger cloud formations at higher levels [44]. The active contour method, as proposed by Chan and Vese [45], represents a promising approach to detecting the SBF by converging a morphological curve to the convective clouds. Building on the work of [46] and [34] [40], this study uses an automated technique based on a snake morphological algorithm to identify SBF clouds in visible band images. This technique is highly efficient, robust and offers superior computational performance than classical techniques listed above. The implementation of the methodology of our study is described below.

### 2.3.1. Snake Algorithm Model

To automatically identify cloud lines associated with SBF without first diagnosing SBF days, as in the example of [34], we use a morphological snake algorithm on satellite images. Active contours or snakes are curves that are developed from an image for the identification of objects in that image [45]. Using a level set approach, [37] [47] used the snake contour which changes gradually by reducing the

functional energy of the snake (Equation (1)).

$$E_{\text{snake}} = E_{\text{inside}} + E_{\text{outside}} \tag{1}$$

where  $E_{\text{inside}}$  and  $E_{\text{outside}}$  are the inside and outside energy of the snake, respectively. Let the contour of the snake be parametrized in a level set as:

$$u(s) = (x(s), y(s)) \text{ and } s \in [0, 1] \tag{2}$$

The speed of curve evolution is defined by an operator, with the curve ultimately evolving towards a local minimum that corresponds to the object's contours. The energy that needs to be minimized is found by the following formula:

$$E(u(s)) = \frac{1}{2} \int_0^1 \left( \alpha \frac{\partial u(s)}{\partial s} + \beta \frac{\partial^2 u(s)}{\partial s^2} \right) ds + \int_0^1 I(u(s)) ds \tag{3}$$

To minimize this energy, apart from the classical methods based on Euler's equations, there are two models for dealing with the temporal evolution of the snake contour using Level-set approaches:

**Geodetic Active Contour (GAC)**

$$\frac{\partial u}{\partial t} = g(I) \cdot |\nabla u| \cdot \text{div} \left( \frac{\nabla u}{|\nabla u|} \right) + g(I) \cdot |\nabla u| \cdot \nu + \nabla_{g(I)} \cdot \nabla u \tag{4}$$

In this model,  $g(I)$  is an edge detector to obtain information about the boundaries of the target object defined by  $g(I) = \frac{1}{1 + |\nabla \hat{I}|^p}$ , where  $\hat{I}$  is a smoothed version calculated using a Gaussian filter and  $p = 1$  or  $2$ . The three terms of the GAC model depend on  $g(I)$ .

**Active Contour Without Edge (ACWE)**

[45] use the Euler-Lagrange equation of the implicit version of the functional differential equation (FDE).

$$\frac{\partial u}{\partial t} = |\nabla u| \left[ \mu \cdot \text{div} \left( \frac{\nabla u}{|\nabla u|} \right) - \nu - \lambda_1 (I - C_1)^2 + \lambda_2 (I - C_2)^2 \right] \tag{5}$$

where:

$$C_1 = \frac{\int_{\Omega} u_0(x, y) H(u(x, y)) dx dy}{\int_{\Omega} H(u(x, y)) dx dy}, \quad C_2 = \frac{\int_{\Omega} u_0(x, y) H(1 - u(x, y)) dx dy}{\int_{\Omega} u_0(x, y) H(1 - u(x, y)) dx dy}$$

and  $H(z)$  is the Heaviside function:  $H(z) = \begin{cases} 1, & \text{if } z \geq 0 \\ 0, & \text{if } z < 0 \end{cases}$

In the ACWE model (Equation (5)),  $I$  is the pixel value of the images;  $\mu$ ,  $\nu$ ,  $\lambda_1$  and  $\lambda_2$  are positive constants and are respectively the interior  $C_1$  and exterior  $C_2$  contours of the object. As  $g(I)$  does not appear in the ACWE model, then the evolution of contours with ACWE would be less dependent on the intensity of the image. To deal with topological changes such as merging and splitting, the Osher-Setian level set method allows the snake curve to be represented implicitly as a level set of an integrating function.

### 2.3.2. Level Set Function $u$ Based on Active Contours

The level set approach is used to capture the contours of objects of interest in an image. The fundamental principle of this method is based on an Eulerian representation of the evolving curve, as outlined in Equation (5). In the field of mathematical morphology, this is regarded as the initial contour, or level 0 line, of a Level Set Function (LSF) [48]. An LSF is a scalar function  $u$  of the space variable that is sufficiently regular. In the classical approach, the inner region, denoted  $\Omega_{int}$ , corresponds to positive levels, while the outer region,  $\Omega_{ext}$ , receives negative values (Figure 2). The curve evolution algorithm comprises the construction of the LSF function from the initial curve  $u(s, t = 0)$ , followed by its evolution in accordance with Equation (6) until convergence is reached [49]. Thereafter, the  $n$ -level curve is extracted. The majority of segmentation methods employ this concept, with the primary objective being to commence with an initial curve that may (or may not) encompass the objects of interest and subsequently evolve it towards a series of levels characterized by a high gradient, thereby delineating distinct regions.

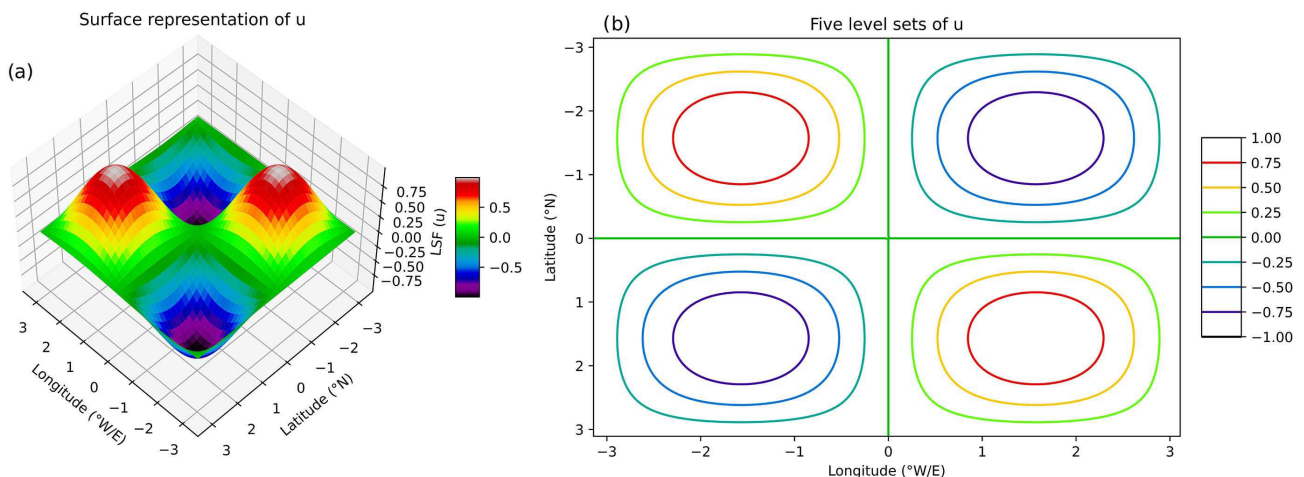


**Figure 2.** Evolution of the level set function  $u$  based on the active contours. (a) Surface representation of the evolution of the initial contours of the snake. (b) The five level sets show that the snake curve follows an outward movement (divergence) with positive values and the interior points take on negative values (convergence) with values close to zero for the boundary curves.

The evolution of the function of all  $u$  levels depends on the active contours. Figure 2 illustrates the initialisation of the snake curve, which progresses outwards with positive values. The sets of five levels shown in Figure 2(b) show that the boundary curves are close to zero, while the interior points take on negative values. When this initialization is used with  $u = 0$ , the conventional meanings of “inside” and “outside” become arbitrary. Furthermore, any C contour can be specified for initialization and it can be observed that initializing the set of levels with a special divergence function (Equation (7)) over a specific area of the image allows stability towards high gradients that characterize the clouds of interest (Figure 4). The functional energy of the snake can therefore be represented by a formulation of the level set, and the problem of minimizing this energy can then be

transformed into the solution of an evolution equation for the level set. By approximating these solutions with morphological operators (contraction and dilation) and by defining the time step, the number of iterations and initializing the Level Set Function (LSF), it is possible to obtain an appropriate smoothing of the curvature.

### 2.3.3. SBF Detection Criteria

To detect clouds associated with SBFs in a grayscale image, we exploit the variations in reflectance (or brightness) that mark the presence of clouds. In this approach, the snake algorithm identifies the brightest regions likely to be associated with clouds by applying the filtering and segmentation techniques described above. The criterion is performed in four steps (**Figure 3**):

- 1) Define an active contour containing the LSF surface levels to which we assign negative values at snake initialisation.
- 2) Evolve the contour on a grayscale image towards convective clouds using morphological operators (dilation and erosion) (**Figure 4**).
- 3) Define a specific region of interest (ROI) inland and parallel to the coastline to facilitate the expansion of the snake towards SBF clouds.
- 4) Define the convergence (or stopping) criterion based on minimizing the functional energies of the snake

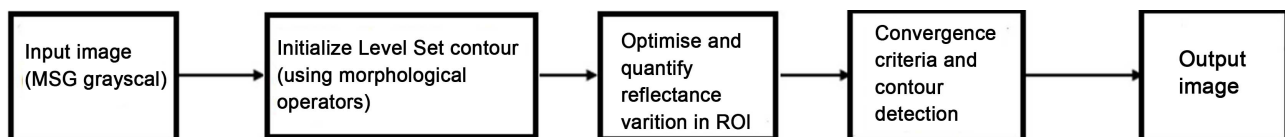


**Figure 3.** Flowchart of the Snake algorithm. It explains the steps of the detection algorithm based on the Snake (or Level Set) approach. Inputs are grayscale images from the MSG sensor. The snake is initialized with morphological operators based on reflectance variation in the ROI.

Morphological operators, such as dilation and erosion, are fundamental tools in image processing, particularly for binary (black and white) images and applications where the shape and structure of objects in an image are important. In a discrete binary function  $u$ , the  $SI_d$  and  $SI_h$  operators perform the same operation; however, the  $SI_d$  operator only operates on white (or active) pixels, while the  $SI_h$  operator only operates on black (or inactive) pixels (**Figure 4(a)**). For each active pixel,  $x_1$ , in a binary image, the  $SI_d$  operator searches for small straight lines (three pixels long) of active pixels that contain  $x_1$ . The search is performed in the four potential orientations corresponding to the four segments of the structuring element. If there are no straight lines, the pixel is rendered inactive (see **Figure 4(b)**). The  $SI_d \circ SI_h$  composition first eliminates the net inactive pixels with  $SI_h$ , then repeats the procedure for the active pixels with  $SI_d$ . The result is a global smoothing of  $u$ , as shown in the first row of **Figure 4** and **Figure 5**. Note that these morphological operators are fundamental to image processing because they provide powerful means of analysing, modifying and extracting important structural information from images. Their conceptual simplicity

and effectiveness make them basic tools in almost all modern image processing applications.

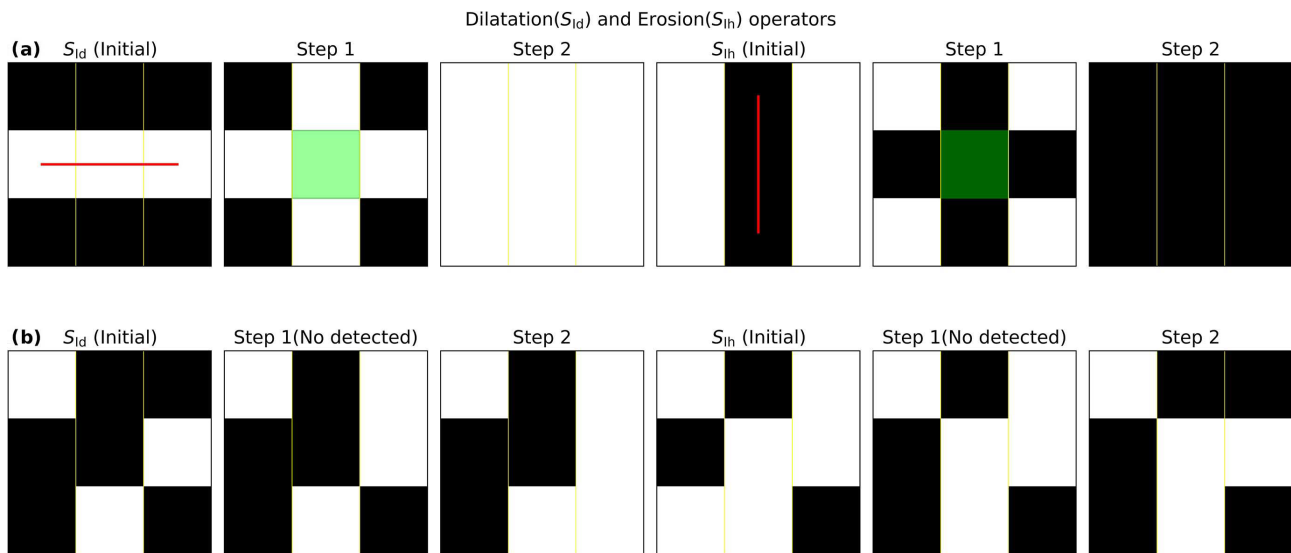


**Figure 4.** Morphological operators. Examples of the action of the  $SI_d$  and  $SI_h$  operators on individual pixels of binary images. (a) Cases where a straight line is found (marked in red), the central pixel remains active (in green). (b) When the central pixel does not belong to a straight line of active pixels, it is rendered inactive.

SBF's detection logic is based on the values of the pixels in the image and on dynamic adaptive thresholds based on the values of the pixels in the image itself, making it adaptable to different lighting or contrast conditions. The specific reflectance dispersion of clouds associated with SBF is calculated in the literature to quantify local reflectance variations in a region of interest (ROI) and defined by:

$$\text{SpecfRef} = \frac{\text{Ref}_{\max} - \text{Ref}_{\min}}{\text{Nonzero pixels}} * \text{Scaling Factor} \quad (6)$$

where  $\text{Ref}_{\max}$  and  $\text{Ref}_{\min}$  have the maximum and minimum reflectance in the ROI respectively.

Here the scaling factor is chosen on the assumption that the clouds associated with the SBF would be the brightest (*i.e.*, a value of 255 on the 256-level grayscale pixel intensity). The method is commonly used in image analysis to standardize reflectance values according to the dynamics of the pixels in the ROI. Depending on the visible band chosen (0.8  $\mu\text{m}$ ) with the solar zenith angle criterion below  $80^\circ$ , we set the brightest pixel limit at  $1.8^\circ$  longitude/latitude in the ROI from the coastline due to the low topography of the region. This is the limit of the ROI points in relation to the coastline. Here  $1.8^\circ$  latitude, or around 200 km from the equator, is chosen to ensure that the analysis zone includes enough points inland while remaining close to the coast. This distance corresponds to a value where the SBF effect is still significant. It is adapted according to the specific characteristics of the region studied (such as the Gulf of Guinea). In this region, SBs can penetrate significantly inland depending on topography (Figure 1), temperature gradients and daytime weather conditions.

### 2.3.4. Regression Methods for Modeling Sea-Breeze Front Isochrones

In order to track the inland propagation of the SBF and investigate its speed, different regression methods approximating the cloud lines are tested. Regressions are used to refine and model the centroid connection curves of the cloud leading edge (*i.e.*, the southern edge), which are used to represent the SBFs, because we're interested in the leading edge of the SB, which is often influenced by south-westerly winds coming off the sea and laden with moisture. The initial approach is a piecewise interpolation method, which connects each pair of points with a straight line. In this way, the central points of the cloud associated with the SBF are identified as individual pixels in a binary image obtained as a result of the segmentation process.

The clouds have been transformed into a set of spatial coordinates, generating a list of the positions ( $x_i, y_i$  coordinates) of the constituent points of the leading edge of the SBF. The clouds have been transformed into this particular coordinate system, and the regressions are applied in this space. The image is then transformed back to lat/lon. However, unlike higher degree splines, such as cubic and polynomial splines, they are unable to capture curvature and can cause angular transitions at interpolation points.

For context, several other regression methods were analyzed, including cubic polynomial regression, moving average regression and kernel-weighted Local Polynomial Regression (kwLPR). The moving average (MA) method involves averaging subsets of adjacent data points, which facilitates data smoothing. This method reduces rapid fluctuations, although it cannot accurately reflect large variations in the reference curve (linear spline calculated by piecewise fitting) and requires a number of data points for calculation. kwLPR is better able to account for local variations in the data, which can be very beneficial in cases where the relationship between variables undergoes changes at different levels within the data set. It is more effective at modeling local variations than global regression methods. Cubic polynomial regression (PolyCubic), which involves fitting a third-degree polynomial curve to the data, is effective in capturing non-linear variations, although it can introduce undesirable oscillations. In contrast, linear regression attempts to fit a straight line to the data, but is unable to capture nonlinear curves or variations.

The following section presents an overview of the concepts associated with kwLPR, nonparametric curve-fitting method. kwLPR and moving weighted averages (local regression, kernel, spline, etc.) are local estimates in which, for each point  $x$  where an approximation is desired, a polynomial model is fitted using the points close to  $x$ . Points close to  $x$  have greater influence on the model fit than points further away. This is achieved by applying a weighted error minimisation function, defined by Gajewicz-Skretna *et al.* [50]:

$$m(x) \approx \sum_{j=0}^p \frac{m^{(j)}(x_0)}{j!} (x-x_0)^j \equiv \sum_{j=0}^p \beta_j (x-x_0)^j \quad (7)$$

This function is applied locally to each point of interest using the weighted least

squares method (also known as kwLPR), which minimizes the number of points of interest. These methods are particularly useful for data sets where the relationship between variables is not adequately represented by a simple global functional form, such as a straight line or a polynomial curve of a fixed degree.

The mean absolute distance error (MAE) is calculated by taking the average of the differences in the absolute distances between the detected reference line and the curves fitted to evaluate the deviation of the regressions from a reference that represents the cloud leading edge centroids. The objective of the regression analysis was to create a model for the centroid connection that would ensure its alignment with the coastline. The centroid reference point is calculated using morphological operators (**Figure 4**). The MAE is calculated as follows:

$$\text{MAE} = \frac{1}{n} \sum_{i=1}^n |y_i - \hat{y}_i| \quad (8)$$

The total number of points in the sample is denoted by  $n$ . The actual value for sample  $i$  is represented by  $y_i$ , while the fitted value for sample  $i$  is denoted by  $\hat{y}_i$ . A lower mean absolute error (MAE) indicates a better approximation of the model, as it implies that the fitted points are, on average, closer to the true points.

### 3. Results

In this session, we present the results of the algorithm implementation in two main parts. The first part consists of identifying appropriate test cases (12 January 2017 and 7 February 2018) among the detected days to demonstrate the capability of the algorithm. In this part, we show the different steps of the algorithm as described in the method section, and then we describe the different regression methods used to implement the optimal approach (kwLPR). The second part includes a diurnal climatological analysis from the period of February (the last dry month before the first rainy season) of the long dry period DJF of 2013–2018 (covering the operational period of METEOSAT-10) in the Gulf of Guinea. The dynamic meteorological characteristics and conditions involved are then assessed.

#### 3.1. Workflow of the Snake Algorithm: A Case Study

##### 3.1.1. Description of the SBF Case

MSG satellite images are used to detect clouds associated with the SBF among the cumulus clouds using automatic detection techniques based on active contours (snake). These automatic techniques use morphological curves that evolve on these gray level images to capture the clouds of interest.

**Figure 5** shows the evolution of the SBF clouds during 12 January 2017, from their initial development to their dissipation. The SBF clouds become visible from 13 UTC (**Figure 5(b)**) and begin to dissipate in the visible images at 17 UTC (**Figure 5(f)**). The images show clear skies over the sea and the development of SBF convective clouds inland along the Guinea coasts. The largely unobscured, cloud-free landscape along the coast on that day helps to locate the SBF and its penetra-

tion inland. In order to assess the characteristics (spatial structure, boundary, shape, etc.) of these detected clouds, the automatic thresholding method based on the evolution of contour lines, which is described in the following, is applied to capture the contours.

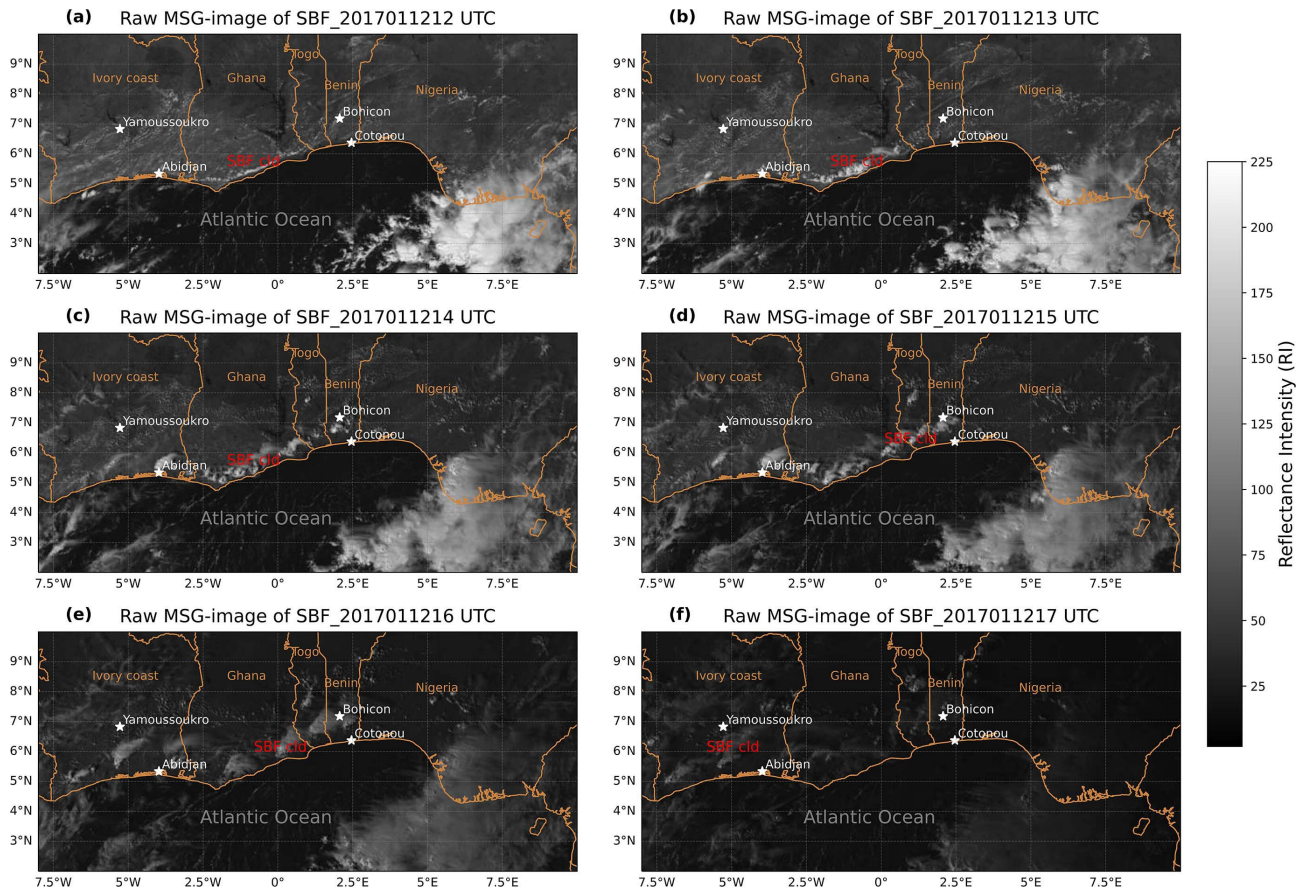


**Figure 5.** Raw MSG images on 12 January 2017 (12–17 UTC) showing SBF evolution from the first clouds development until their dissipation ((a) to (f)). The SBF cloud line is most visible from 13 UTC to 16 UTC ((b), (e)) and dissipates at 17 UTC (f).

### 3.1.2. Automatic Segmentation of MSG Images for Convectives and SBF Clouds Detection

In image segmentation, active contours are dynamic curves that move towards the boundaries of the object. To capture the contours, we explicitly defined external forces (morphologic operators) that can move the zero-level set curve towards the cloud boundaries.

The snake curve moves and slowly follows the contours of the clouds as a function of various parameters such as elasticity, noise tolerance and regularity. The curve evolves iteratively until it is positioned in the image, more precisely in the vicinity of the shape to be detected, with an initial contour that undergoes deformation under the effect of several forces (energies). The spatial propagation of the curve over time is carried out using the level set numerical method used to minimize these energies. (See **Figure 6**)

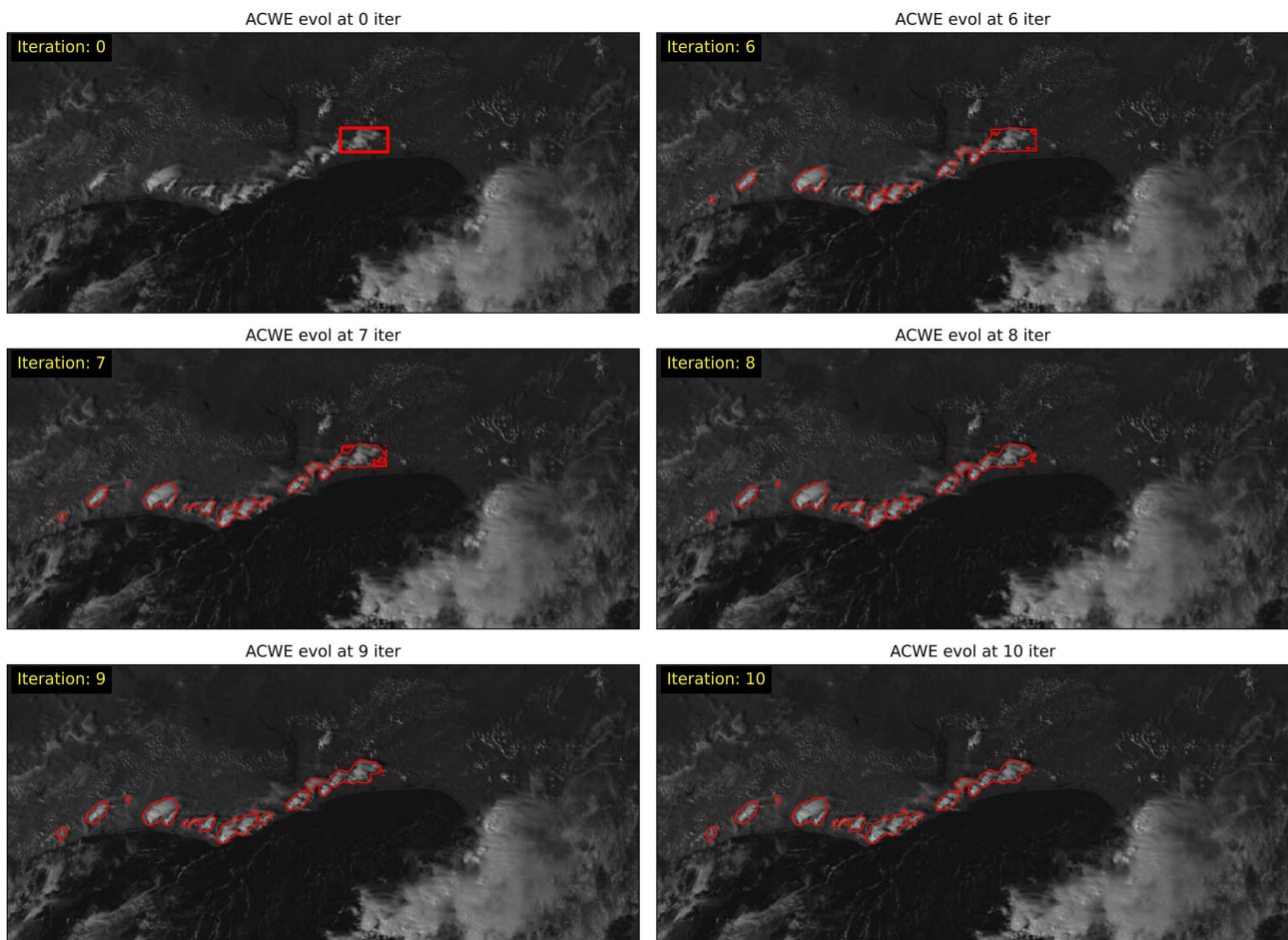


**Figure 6.** Evolution of the Active Contour Without Edge (ACWE) on the MSG image. Results after 10 iterations. The snake is often initialized near the objects of interest and evolves towards the bright clouds thanks to the balloon forces (dilation and erosion) from the 10th iteration and then encircles the edges of the clouds.

The functional energy of the snake can therefore be represented by a level set formulation, and the problem of minimizing this energy can then be transformed into the solution of a level set evolution equation. By approximating these solutions with morphological operators with an optimal initial parameterisation of the snake, an appropriate smoothing and convergence of the curvature is performed. Subsequently, the above approach was automatically applied to gray-scale MSG images in order to detect cumulus clouds parallel to the coast and associated with the SBF along the Gulf of Guinea (**Figure 7**). To accurately detect convective clouds from these images, we first initialize an active contour (or snake) in the vicinity of the objects by defining LSF surface levels to which binary values are assigned to promote the expansion of the snake. The contour then evolves progressively on the grayscale image, approximating the SBF clouds with morphological operators such as dilation and erosion (see the operators in **Figure 4** and Appendix).

To improve detection accuracy, we define a specific region of interest (ROI), located inland and parallel to the coast (red band of the coastal zone on **Figure 1**),

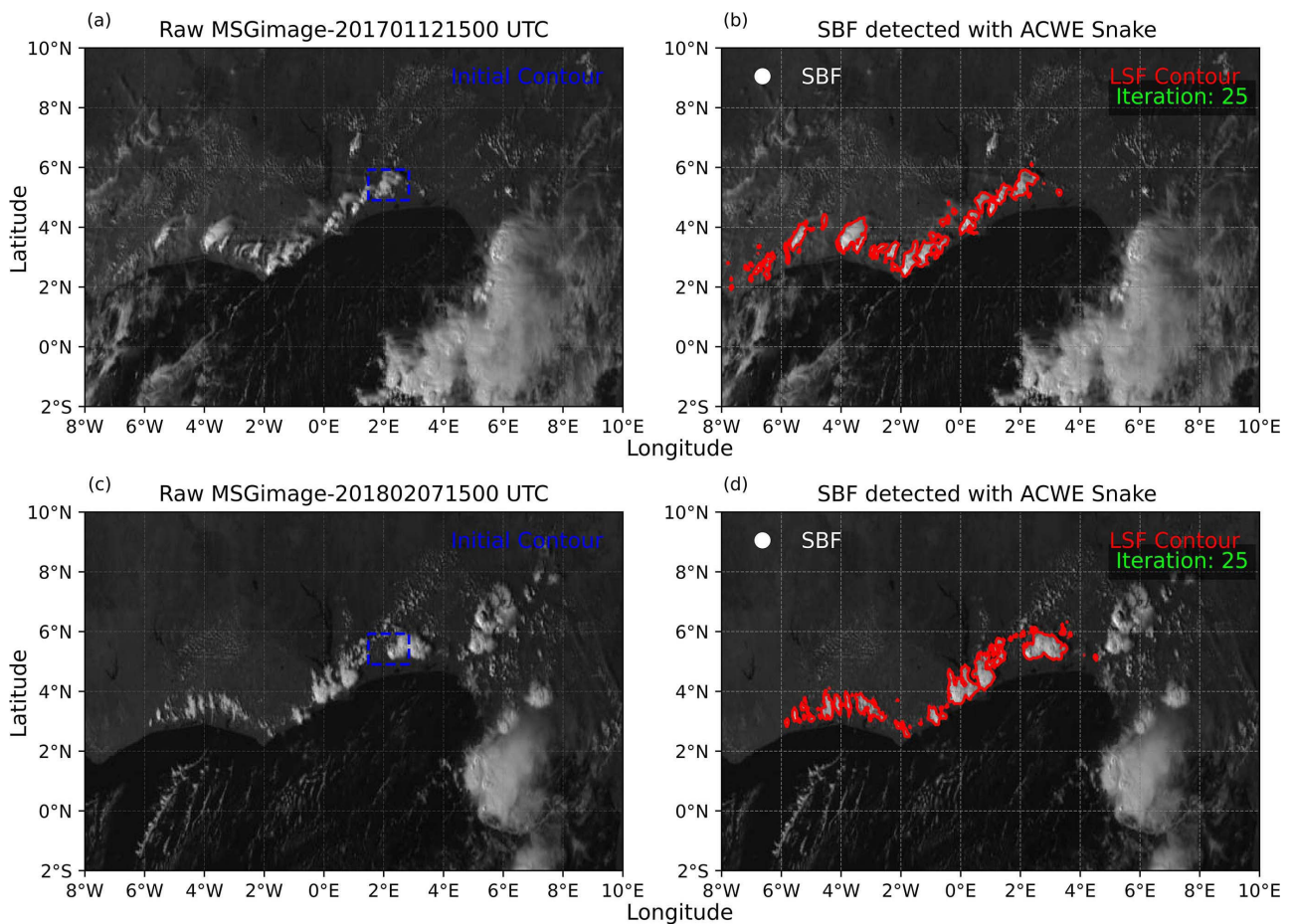


**Figure 7.** SBF detected after 25 iterations during the evolution of the snake on 12 January 2017 (a), (b) and 7 February 2018 at 15 UTC (c), (d). The initial blue contour should be in the ROI and close to the clouds (a), (c). Its evolution over time is based on the level set function (LSF), red contour (b), (d) and automatically adjusts to capture SBF clouds.

which restricts the analysis to relevant areas. Finally, we optimize the detection conditions by taking into account the acquisition time of each image, thus ensuring better adaptation to temporal variations in the SBF. Next, the segmented images are binarised using the LSF function, which is based on dynamic adaptive thresholds for an image as a function of the percentile of pixel values in the image itself. This process enables the image to be adapted to different lighting or contrast conditions. SBF detection is therefore based on the evolution of a parametric curve towards strong image gradients from a specific dispersion function, which is used to quantify reflectance variations in the ROI.

### 3.1.3. Automatic Detection of the Cloud Line Associated with the SBF

Automatic detection of SBF clouds among low cumulus clouds can be difficult due to their similar characteristics. To achieve this, the automatic morphological snake algorithm used is well suited to capturing the spatial structure and temporal evolution of these clouds. Identifying these cloud patterns in MSG images would be interesting for determining how far the SBF propagates inland without the need for local probes, as in the case of Ferdiansyah *et al.* [34]. In addition, almost all

existing methods for detecting sea-breeze front systems have been carried out manually. It is therefore obvious that an automatic approach would facilitate this tedious manual task of extracting SBF structures. In order to achieve this, we have employed morphological snake techniques to identify clouds associated with SBFs in greyscale MSG images, using the variations in reflectance (or brightness) that are characteristic of cloud presence. The algorithm identifies the brightest regions, which are likely to be associated with SBF clouds, through the application of filtering and segmentation techniques as previously described.

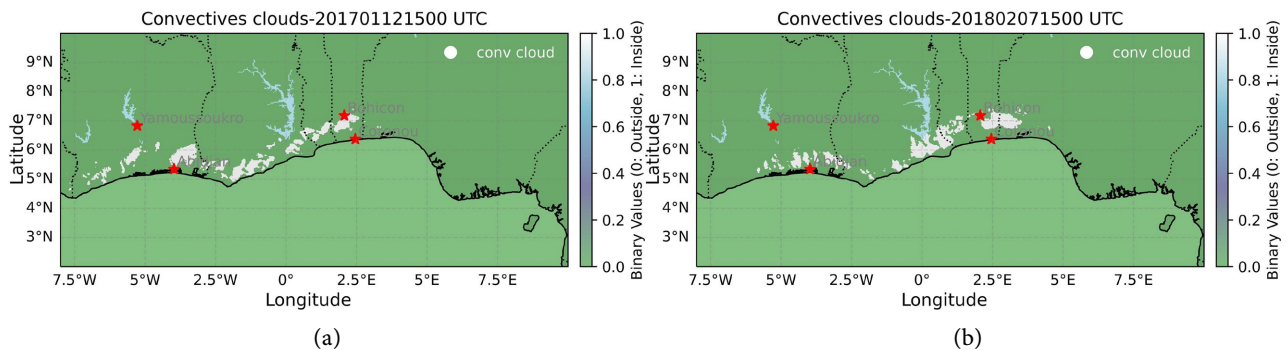


**Figure 8.** Convectives clouds detected by the algorithm on 12 January 2017 and 7 February 2018. Convective clouds are detected from the segmented level set function via a binary criterion where 0 (green color) indicates the outside with any other non-cloud object and 1 (white color) indicates the inside of the snake contours that represent the convective clouds of interest. The red stars are the coastal and interior stations of the ROI zone over which we will later assess SBF propagation.

**Figure 8** illustrates the algorithm's capacity to accurately identify the convective clouds detected on 12 January 2017 by the snake algorithm based on a segmented level function and a binary criterion. The segmentation performed by the algorithm effectively isolates the cloudy areas in white, which correspond to potential convective clouds, while those in green represent the outside of the contours defined by the model. Binary detection simplifies interpretation: everything that is 1 is considered to be convective clouds, while 0 represents everything that is not, allowing us to focus only on regions that are relevant to the study of convective clouds associated with SBF in the area of interest. These results form an essential basis for assessing the interaction between these clouds and the propagation of SBFs. The arrangement of red star stations makes it possible to distinguish between the effects of SBFs on coastal areas and more inland areas.

In these areas, the difference in temperature between the ocean surface and the continental coast creates a thermal gradient that facilitates the formation of SBF on land. As illustrated in the raw MSG image (**Figure 9(b)**), the absence of clouds is indicated by the black areas in the satellite images. To the southwest, a vast area of clear sky can be observed along the Guinean mainland coast, extending over several kilometers. This area is subject to the influence of the SB, or maritime influx. **Figure 9(b)** illustrates the formation of SBF clouds (blue) in conjunction with the predominance of south-westerly winds and the presence of clear skies along the Gulf of Guinea.

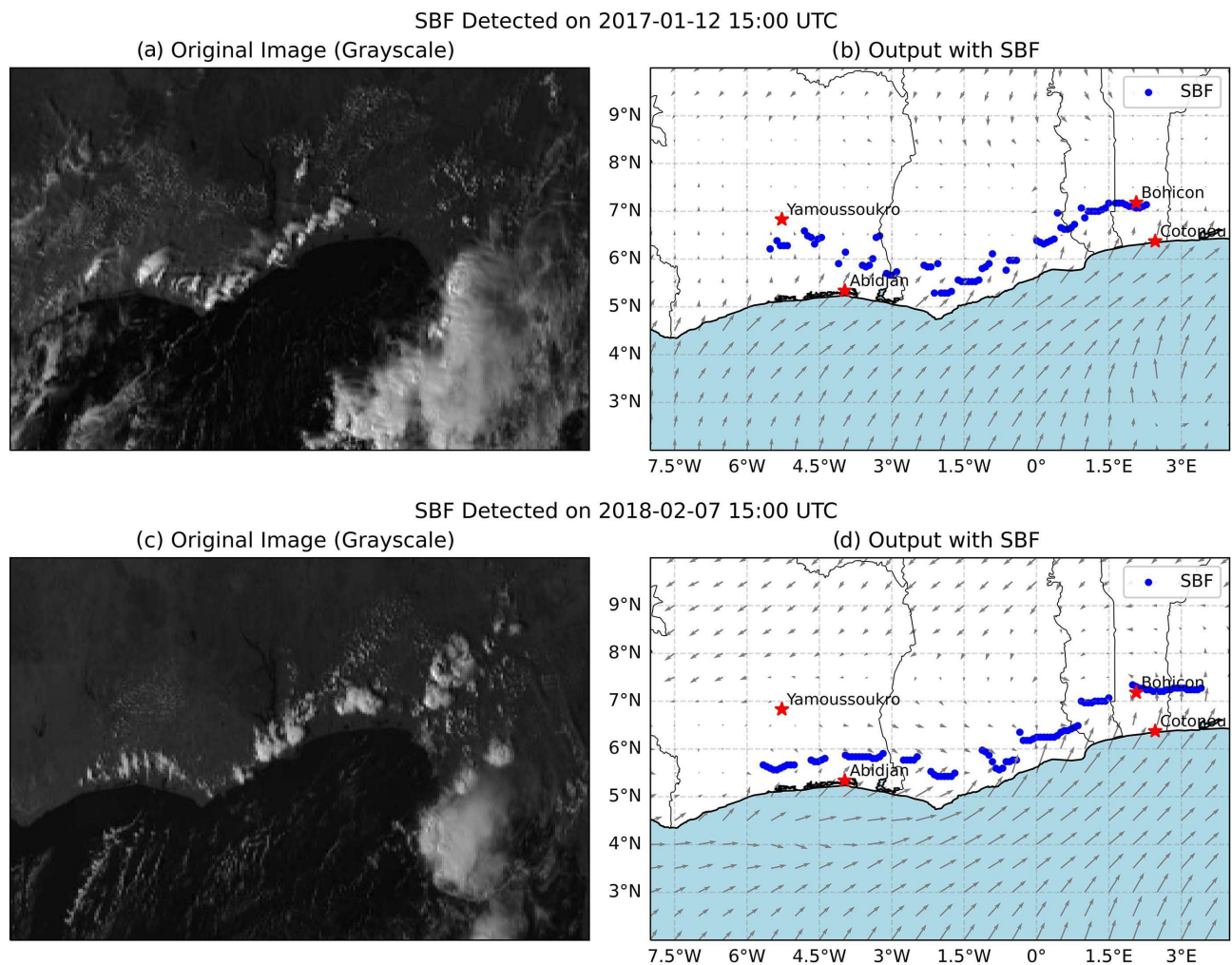


**Figure 9.** SBF detected by the algorithm on 12 January 2017 and 7 February 2018. SBF clouds are automatically detected in the ROI using filters based on the reflectance values of the MSG images. The coordinates of each detected pixel are adjusted to obtain the pixel center points. The centroids are then filtered to retain only those located within  $1.8^\circ$  (longitude/latitude) of the coastline with specific geographical conditions. SBF clouds begin to form at 12 UTC and move parallel to the coast gradually moving away in the afternoon from 13 UTC, dissipating at 17 UTC.

**Figure 9(b)** and **Figure 9(d)** show the SBF clouds detected on 12 January 2017 and 7 February 2018, respectively. Cloud alignment is more pronounced in this area, where SB winds influence SBF formation. The clouds associated with SBFs are detected on the basis of the reflectances that indicate the presence of clouds. In this approach, the snake algorithm identifies the brightest regions likely to be associated with SBF clouds by applying filtering and binarisation techniques. To identify the coordinates of the pixels in the binary image, filtering is performed. The coordinates of each pixel detected are adjusted to obtain the central points of the pixels. The central points are then filtered to retain only those located within  $1.8^\circ$  (longitude/latitude) of the coastline SB influence zone). The aim of this selection is to focus on the geographical ROI, excluding points located over the ocean which are not relevant to the SBF clouds. Finally, a binary mask is applied to retain only the points located inland above the coastline. These techniques help to work

with a precise location of the clouds associated with SBF by selecting the relevant pixels and applying strict geographical conditions to retain only points above the coast and in the ROI.

## 3.2. Evaluation of Different Interpolation Methods for SBF Isochrones

### 3.2.1. Comparative Analysis of Different Regression Methods for the Fitting of SBF Isochrones

The SBF is defined by the appearance of a line of cloud which roughly follows the shape of the coastline. To model this line and find the one that is subjectively closest to reality, we carried out a comparative analysis of several regression methods (linear, cubic polynomial, moving average and kernel-weighted local polynomial) for spline fitting.

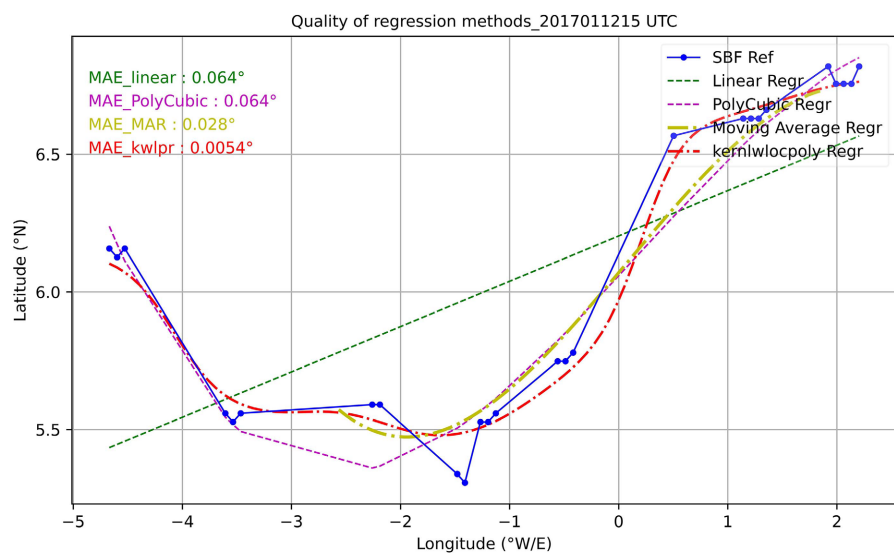


**Figure 10.** Regression method for spline fitting. The blue curve with blue dots represents the reference positions of the SBF clouds. The reference curve serves as a point of comparison for the other regression methods, which are represented by the dotted line. The red curve represents kernel-weighted local polynomial regression (kwLPR), the yellow curve is weighted moving average, the green curve is linear regression and magenta is cubic polynomial regression.

The idea here is to present a fit of the points connecting the centroids of the leading edges of clouds associated with SBFs. This avoids unwanted curvatures and oscillations and gives an idea of the extension and organization of the points. The connection of the points indicated by the blue color (centroid of the leading edge of SBF clouds) is determined using a simple piecewise linear fit, based on line segments (Figure 10). Linear splines enable these points to be connected in a simple way. By connecting the points with line segments, we obtain an approximation of the front line, while retaining the necessary simplicity and accuracy. This adjustment establishes a link between the central points of the cloud leading edges, reflecting local variations. It should be noted that the points in question are subject

to variations that we will try to improve by means of other more robust than linear regressions. **Table 2** shows the mean absolute distance error values calculated from these different methods.

**Table 2.** Mean absolute distance error values for each time step for the different regression methods.

Time (UTC)	Mean Absolute Distance Error (MAE in degree)					
	12	13	14	15	16	17
PolyCubic	0.056	0.056	0.056	0.056	0.056	0.056
MA	0.021	0.021	0.021	0.021	0.021	0.21
KwLPR	0.0021	0.0026	0.0041	0.0054	0.0032	0.0032

The kernel-weighted local polynomial regression (kwLPR) method was found to offer the most accurate results of the evaluated methods, with a mean absolute distance error (MAE) of 0.0034° on average. This is a superior result to the other models, which offer 0.056° and 0.021° respectively for the cubic polynomial regression (PolyCubic) and moving average (MA) methods (**Table 2**). This value for kwLPR indicates that the kernel-weighted local polynomial regression method is a well-balanced approach, capable of reducing errors while tracking variations in the reference curve.

### 3.2.2. Inland Propagation of SBF on 12 January 2017

The propagation of the SBF in time and space provides a better understanding of the processes involved in its evolution and its interaction with the coastal environment. The kwLPR curve proved to be the best regression method, enabling us to carry out this study using hourly isochrones (**Figure 11(a)**).

The Gulf of Guinea has an essentially flat west-east coastline. This favours perpendicular propagation of the SBF along the coast, penetrating deeper inland than in regions where the coast is more irregular. **Figure 11** illustrates the spatio-temporal propagation of the SBF along the Gulf of Guinea. The isochron curves smoothed by the kwLPR technique show that the horizontal trajectory of the SBF follows the coastline with moderate variations in distance from the coast depending on the time of day. From 13 UTC in the afternoon, as the land surface warms, the SBFs advance and penetrate inland under the influence of south-westerly winds. The isochrones show different positions in relation to the coast, indicating that the speed of propagation of the SBF varies from one region to another. In some regions, such as Ghana, the presence of Lake Volta has an influence on the propagation of the SBF, as shown in **Figure 11(a)** (where ripples can still be seen opposing the movement of the isochron curves in the region). The black isochronous line marks the start of SBF formation at 13 UTC and the yellow line its dissipation at 17 UTC. In order to assess the inland propagation of the SBF line, we employed the maximum penetration distance of the isochrone lines from the coast (**Figure 11(b)**). The maximum penetration is calculated using the points furthest

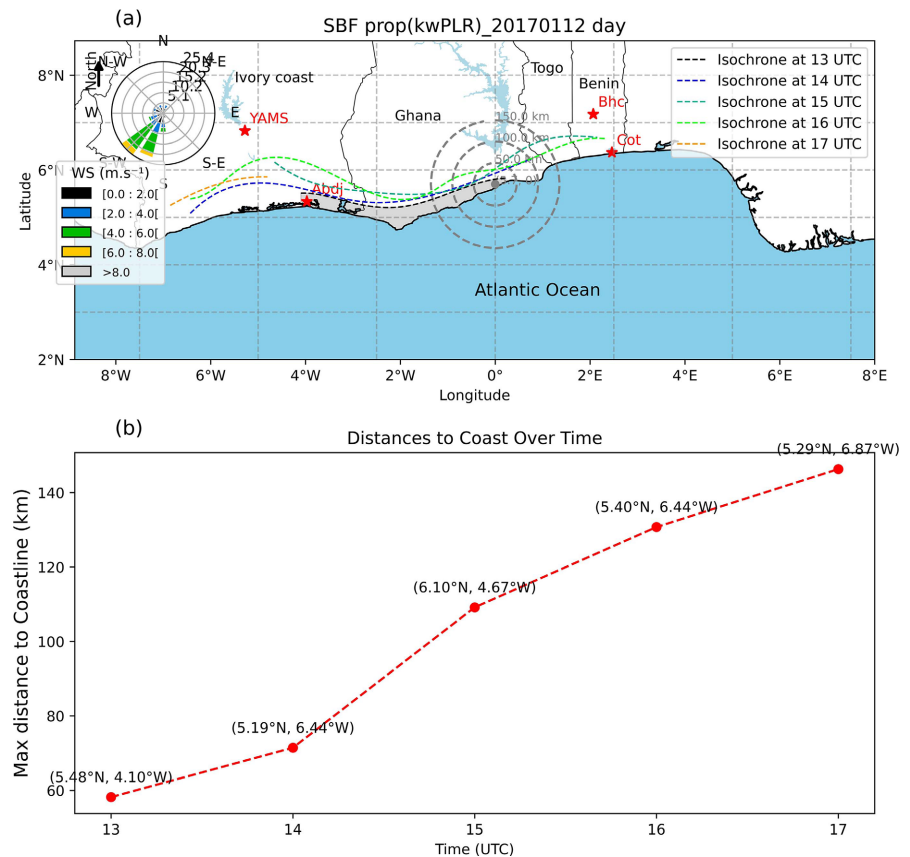


**Figure 11.** Spatial and temporal evolution of SBF along the Gulf of Guinea. Propagation occurs northwards from the coast in SB wind conditions (wind rose on the left) (a). The black isochrone line delineates the start of SBF formation at 13 UTC, when wind speed was minimal ( $2 \text{ m}\cdot\text{s}^{-1}$ ), and its subsequent progression across the continent as wind speed increased ( $6 \text{ m}\cdot\text{s}^{-1}$ ) until dissipation at 17 UTC. The shading between the coastline and the black isochrone is a zone of SBF influence (maritime inflow) at 13 UTC that extends between  $4^\circ\text{W}$  and  $0^\circ\text{E}$ . (b) Maximum SBF penetration is observed in the prevailing SW wind direction, with a maximum of 146.3 km at 17 UTC. Average penetration along the coast from 13 UTC to 17 UTC is 103.17 km.

from the coast from the start of SBF development until its dissipation at 17 UTC. **Figure 10(b)** illustrates the maximum distance between the SBF and the coast at varying times of day (from 13 UTC to 17 UTC). The curve demonstrates a gradual increase in the maximum distance between the SBF and the coast over time. This suggests that the SBF propagates continuously inland throughout the day. There is a relatively modest increase in distance, followed by a marked acceleration between 15 UTC and 16 UTC. SBF penetration also varies according to local topography (**Figure 1**). In high-altitude areas, the progression of the front is often slowed down, as hills and reliefs form physical obstacles that dissipate the energy of the maritime air flow. On the other hand, in flat or low-lying areas, the SBF can penetrate more deeply and at greater speed, reaching greater maximum distances. The maximum SBF penetration is observed in the prevailing SW wind direction, with a maximum of 146.3 km at 17 UTC. Average penetration along the coast

from 13 UTC to 17 UTC is 103.17 km.

This area (Gulf of Guinea), which is subject to marine inputs, is also characterised by inland convective activity which keeps cloud formations close to the coast. It is characterised by a humid tropical climate with high humidity. These conditions can modulate the speed and vertical propagation of the SBF, increasing its capacity to trigger convective thunderstorms in the late afternoon. By favouring convection, the SBF contributes to increasing local rainfall, which in one way or another impacts tropical ecosystems and agriculture.

### 3.3. Analysis of SBF Characteristics over the February 2013-2018 Period

The snake algorithm implemented is capable of automatically scanning all the images from the DJF 2013-2018 period (*i.e.*, 6 years) to automatically detect several SBF events. To do this, we are able to conduct a quantitative study based on statistics to obtain time intervals, frequency and duration of SBF events detected during the month of February of the entire period that represents the month of transition to the first rainy season.

#### 3.3.1. Frequency of Occurrence by Time Class of SBF Events

In February, the climatological analysis of the cases studied examined the characteristics of the SBF events detected. The frequency of occurrence corresponds to the total number of SBF events observed during the period 2013-2018. The start time refers to the time when SBF events are first detected by the algorithm, while the end time indicates the time when they disappear, generally far from the coast. The duration corresponds to the time between the appearance and disappearance of the SBFs, all expressed in UTC hours. Finally, a statistical table of all the cases during the period will be presented.

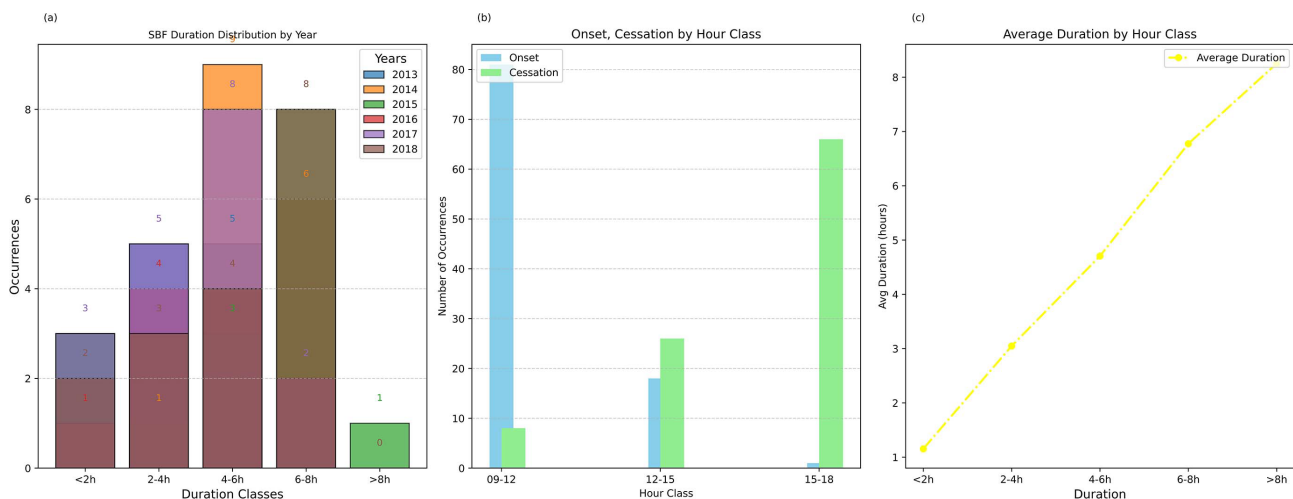


**Figure 12.** The numbers marked on (a) represent the number of occurrences (or frequency) of the different duration classes for each year. Each bar indicates how many times an SBF event was detected in a specific duration range (<2 h, 2 - 4 h, 4 - 6 h, 6 - 8 h, >8 h). (b) shows the frequency of SBF onset and cessation times by each time class and the yellow dotted curve indicates the average duration of SBF events for each duration class. (c) indicates the average duration of SBF events for each duration class.

Of the 95 SBF events, 3 class intervals of onset and cessation times were determined, namely 09 - 12 UTC, 12 - 15 UTC and 15 - 18 UTC, and are presented graphically in **Figure 12(b)**. SBF onset on the Gulf of Guinea coast was dominant at 09 - 12 UTC, with a frequency of about 80%, and cessation at 15 - 18 UTC with a frequency of about 67.5%. The dotted yellow curve shows that the average duration varies from one duration class to another, with the “2 - 4 h” class having a lower average duration than the “6 - 8 h” class in **Figure 12(c)**. This gives a general idea of the trend in durations for SBF events in each class. It should be noted that these times may be related to the fact that we have only used visible images, as the cessation may extend beyond 18 UTC, but is not captured by visible images at the beginning of the night.

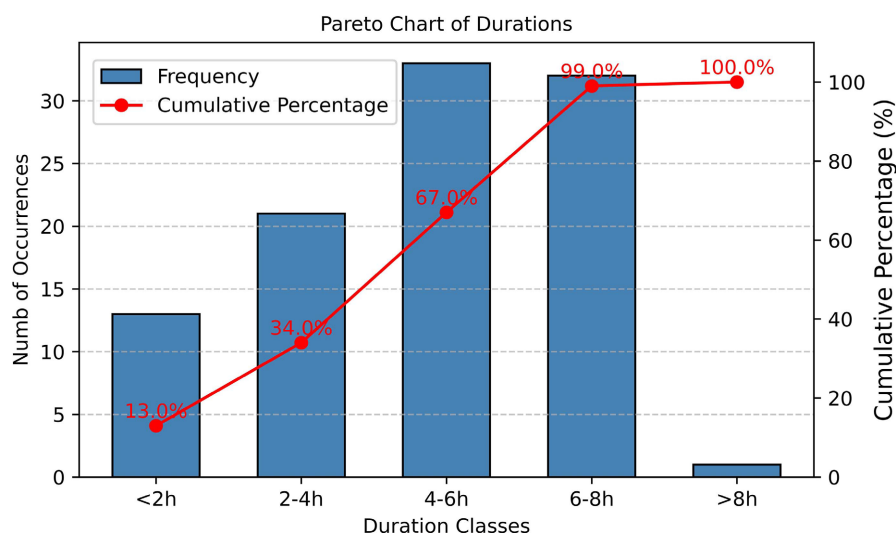


**Figure 13.** Pareto diagram. The diagram shows the frequencies of the categories (duration classes) ordered in descending order. The cumulative percentage of frequencies shows the accumulation of category contributions to the total, and the red curve indicates the cumulative percentage on a scale from 0% to 100%.

**Figure 13** highlights the frequencies of the duration class categories, combining two levels of information (frequency and cumulative percentage). The Pareto chart is based on the Pareto principle or 80/20 rule, which states that 80% of the effects come from 20% of the causes. We use it here to identify the most significant events. In **Figure 13**, the 4 - 6 h and 6 - 8 h duration classes represent the majority of occurrences, and 80% of cases come from these categories. It also shows the low-contribution categories, which are often less relevant for analysis, and provides a powerful visualisation for prioritising and deciding where to focus our analyses. In our case, it allows us to distinguish the critical durations when SBF convective clouds form. As we plan to explore the impact of SBF events on convective precipitation, the diagram shows where to focus our analyses in further research. In general, SBF over the Gulf of Guinea coast from February 2013 to 2018 occurred between 15 UTC and 18 UTC. The earliest SBF occurs at 09 UTC and the latest at 18 UTC. The SBF can last from 3 h to 7 h, with the longest dura-

tion being around 8.25 hours.

### 3.3.2. Statistics of Automatic Detection of SBF Days from DJF 2013 to 2018

The algorithm is used to analyse the period from December, January to February (*i.e.*, the main dry season) of each year over the period 2013-2018. The statistical results are presented in the table and diagrams below:

**Table 3.** Statistics of SBF scenes in the MSG satellite images in December-January-February (DJF) from 2013 to 2018.

Months	MSG images analyzed	Nb. of cloud cover images V	Nb. of SBF images	Nb. SBF days
Dec	17825	1768	759	41
Jan	17262	1991	657	34
Feb	16118	2389	1625	95
<b>Summary</b>	51205	6148	3041	170

A summary of the statistical data relating to days with cloud cover and days with SBFs, which were automatically detected by the algorithm during the December-January-February (DJF) period between 2013 and 2018 is presented in **Table 3**. The data demonstrate that of the 170 days with SBFs identified during the December-January-February period, 95 were observed in February, in comparison to 41 and 34 days in December and January, respectively. Furthermore, on days with cloud cover, 68% of SBF images were detected in February, compared with 43% and 33% in December and January, respectively. This discrepancy indicates that February is a considerably more conducive month for the formation of SBF convective systems, with a greater prevalence of regular cloud cover along the coastline.

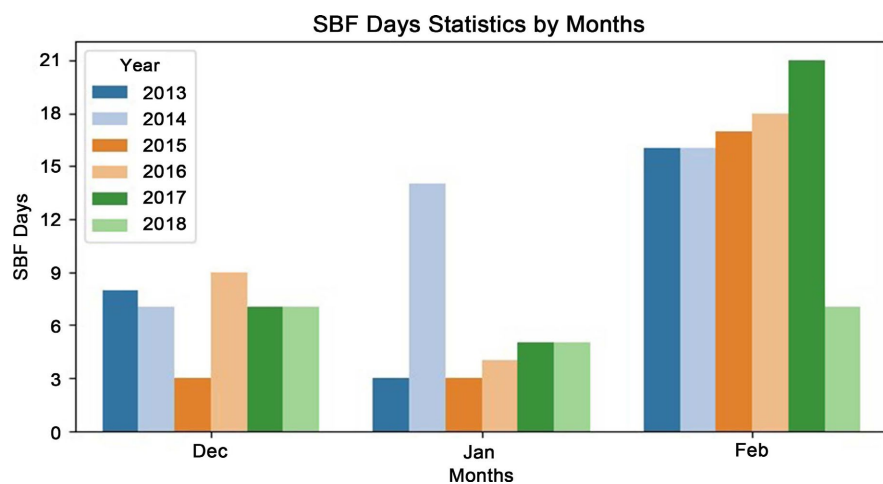


**Figure 14.** Statistics of SBF days by months for the period 2013-2018. February recorded more SBF days with a higher score between 2015 and 2017. January and December recorded the lowest number with a peak in January 2014.

The algorithm is capable of automatically detecting a certain number of SBF days during the DJF months of each year. These days are more frequent in February than in the other two months (December-January) (**Figure 14**). The relevant statistics are shown in **Table 3**, which illustrates the number of SBF days per month of each year. In January, the discrepancy observed would be due to a large number of images detected in which large-scale convective clouds with irregular shapes masking the SBF are very sensitive to the algorithm.

The algorithm used in this study effectively captures the structure and evolution of SBF clouds, offering a robust and faster alternative to manual detection methods such as those used in [15]. Its flexibility allows it to be applicable in different domains using images as input and to detect textured patterns in grayscale images in a shorter time compared to the work of [35]. It is therefore a promising avenue of research, as it is a fast and robust computational approach with flexible application.

#### 4. Conclusions

This paper presents an automatic method for detecting sea breeze fronts (SBFs) from Meteosat satellite imagery in the Gulf of Guinea, West Africa. Currently, the techniques used to analyse sea and land breeze systems in this region are based on observational data and require improvement. The aim is to develop an automatic method that is more robust than traditional manual methods. The method is based on the identification of convective cloud lines as SBF indicators. To do this, the morphological snake algorithm is applied to visible-band MSG satellite images taken every 15 minutes of DJF over the period 2013-2018. This algorithm uses a level set approach and morphological operators to track the evolution of cloud lines as a function of local reflectance variations. The inland propagation lines are adjusted using regression techniques, specifically modelling the connection of the leading edge of the clouds (southern edge), which are influenced by the moist marine winds from the southwest. The effectiveness of the algorithm was tested on two events characterised by well-defined cloud lines and optimal observation conditions. The algorithm successfully detected all clouds associated with SBFs and excluded those over the sea. The results show that the kwLPR approach provided the most accurate approximation, with a mean absolute distance error of  $0.0034^\circ$ . The SBF penetrated as far as 100 to 146.3 km inland at certain longitudes. Its average penetration along the coast is 103.17 km, leaving a clear zone between the SBF clouds and the coast. This zone favours the appearance of specific convergence zones, conducive to the development of convective thunderstorms.

The automatic method used in this study signifies a promising avenue for future research, as it is a rapid and robust approach that is versatile in its application and has the potential to be adapted to numerous other domains. The algorithm has the capacity to identify additional textured patterns in diverse image types. It has demonstrated the capability to automatically detect numerous SBF days in a short time from a substantial number of MSG images. However, the method is limited

to cases where SBFs are accompanied by visible cumulus lines, excluding clear-sky situations where SBFs could also occur. A future analysis could include LBF and clear sky cases to overcome this limitation. Given the prevalence of SBFs in mid-latitude tropical coastal regions with flat topography and seasonal variations, the method could be applied globally in regions with similar characteristics. The subsequent objective is to assess the contribution of SBFs to convective precipitation, with a view to improving regional climate models.

## Acknowledgements

The authors want to thank the BMBF (“Bundesministerium für Bildung und Forschung”) for funding the PhD research of Thomas D. Allagbe through FURIFLOOD Research Project (“Current and future risks of urban and rural flooding in West Africa”, Grant No.: 01LG2086B) under the West African Science Service Center on Climate Change and Adapted Land Use (WASCAL) program. We would like to thank the advisors and examiners for their valuable contributions and comments, in particular Prof Andreas H. Fink and Dr Marlon Maranan from Karlsruhe Institute of Technology (Germany), and the anonymous researchers of FURIFLOOD.

## Conflicts of Interest

The authors declare no conflict of interest.

## References

- [1] Atkins, N.T. and Wakimoto, R.M. (1997) Influence of the Synoptic-Scale Flow on Sea Breezes Observed during Cape. *Monthly Weather Review*, **125**, 2112-2130. [https://doi.org/10.1175/1520-0493\(1997\)125<2112:iotssf>2.0.co;2](https://doi.org/10.1175/1520-0493(1997)125<2112:iotssf>2.0.co;2)
- [2] Simpson, J.E. (1994) Sea Breeze and Local Wind. Cambridge University Press.
- [3] Miller, S.T.K., Keim, B.D., Talbot, R.W. and Mao, H. (2003) Sea Breeze: Structure, Forecasting, and Impacts: SEA BREEZE. *Reviews of Geophysics*, **41**, 1011. <https://doi.org/10.1029/2003rg000124>
- [4] Atkinson, B.W. (1995) Sea Breeze and Local Wind. by J. E. Simpson. Cambridge University Press. 1994. Pp. 234. Price £29.95 (Hardback). ISBN 0 521 452112. *Quarterly Journal of the Royal Meteorological Society*, **121**, 742-742. <https://doi.org/10.1002/qj.49712152315>
- [5] Pearce, R.P. (1955) The Calculation of a Sea-Breeze Circulation in Terms of the Differential Heating across the Coastline. *Quarterly Journal of the Royal Meteorological Society*, **81**, 351-381. <https://doi.org/10.1002/qj.49708134906>
- [6] Planchon, O. and Cautenet, S. (1997) Rainfall and Sea-Breeze Circulation over South-Western France. *International Journal of Climatology*, **17**, 535-549. [https://doi.org/10.1002/\(sici\)1097-0088\(199704\)17:5<535::aid-joc150>3.0.co;2-l](https://doi.org/10.1002/(sici)1097-0088(199704)17:5<535::aid-joc150>3.0.co;2-l)
- [7] Fan, J., Zhang, R., Li, G. and Tao, W. (2007) Effects of Aerosols and Relative Humidity on Cumulus Clouds. *Journal of Geophysical Research: Atmospheres*, **112**, D14204. <https://doi.org/10.1029/2006jd008136>
- [8] Banta, R.M., Senff, C.J., Nielsen-Gammon, J., Darby, L.S., Ryerson, T.B., Alvarez, R.J., *et al.* (2005) A Bad Air Day in Houston. *Bulletin of the American Meteorological*

- Society*, **86**, 657-670. <https://doi.org/10.1175/bams-86-5-657>
- [9] Caicedo, V., Rappenglueck, B., Cuchiara, G., Flynn, J., Ferrare, R., Scarino, A.J., *et al.* (2019) Bay Breeze and Sea Breeze Circulation Impacts on the Planetary Boundary Layer and Air Quality from an Observed and Modeled DISCOVER-AQ Texas Case Study. *Journal of Geophysical Research: Atmospheres*, **124**, 7359-7378. <https://doi.org/10.1029/2019jd030523>
- [10] Wang, B., Geddes, J.A., Adams, T.J., Lind, E.S., McDonald, B.C., He, J., *et al.* (2023) Implications of Sea Breezes on Air Quality Monitoring in a Coastal Urban Environment: Evidence from High Resolution Modeling of NO<sub>2</sub> and O<sub>3</sub>. *Journal of Geophysical Research: Atmospheres*, **128**, e2022JD037860. <https://doi.org/10.1029/2022jd037860>
- [11] Kollias, P., McFarquhar, G.M., Bruning, E., DeMott, P.J., Kumjian, M.R., Lawson, P., *et al.* (2024) Experiment of Sea Breeze Convection, Aerosols, Precipitation and Environment (ESCAPE). *Bulletin of the American Meteorological Society*, **106**, E310-E332. <https://journals.ametsoc.org/view/journals/bams/aop/BAMS-D-23-0014.1/BAMS-D-23-0014.1.xml>
- [12] Suresh, R. (2007) Observation of Sea Breeze Front and Its Induced Convection over Chennai in Southern Peninsular India Using Doppler Weather Radar. *Pure and Applied Geophysics*, **164**, 1511-1525. <https://doi.org/10.1007/s00024-007-0234-3>
- [13] Wu, S., Sakaeda, N., Martin, E., Rios-Berrios, R. and Russell, J. (2024) The Contribution of Mesoscale Convective Systems to the Coastal Rainfall Maximum over West Africa. *Monthly Weather Review*, **152**, 1787-1802. <https://doi.org/10.1175/mwr-d-23-0148.1>
- [14] Planchon, O., Damato, F., Dubreuil, V. and Gouery, P. (2006) A Method of Identifying and Locating Sea-breeze Fronts in North-Eastern Brazil by Remote Sensing. *Meteorological Applications*, **13**, 225-234. <https://doi.org/10.1017/s1350482706002283>
- [15] Anjos, M. and Lopes, A. (2018) Sea Breeze Front Identification on the Northeastern Coast of Brazil and Its Implications for Meteorological Conditions in the Sergipe Region. *Theoretical and Applied Climatology*, **137**, 2151-2165. <https://doi.org/10.1007/s00704-018-2732-x>
- [16] Muppa, S.K., Anandan, V.K., Kesarkar, K.A., Rao, S.V.B. and Reddy, P.N. (2012) Study on Deep Inland Penetration of Sea Breeze over Complex Terrain in the Tropics. *Atmospheric Research*, **104**, 209-216. <https://doi.org/10.1016/j.atmosres.2011.10.007>
- [17] Garratt, J.R. (1985) The Inland Boundary Layer at Low Latitudes. *Boundary-Layer Meteorology*, **32**, 307-327. <https://doi.org/10.1007/bf00121997>
- [18] Abatan, A.A., Abiodun, B.J. and Omotosho, B.J. (2013) On the Characteristics of Sea Breezes over Nigerian Coastal Region. *Theoretical and Applied Climatology*, **116**, 93-102. <https://doi.org/10.1007/s00704-013-0931-z>
- [19] Coulibaly, A., Omotosho, B.J., Sylla, M.B., Coulibaly, A. and Ballo, A. (2019) Characteristics of Land and Sea Breezes along the Guinea Coast of West Africa. *Theoretical and Applied Climatology*, **138**, 953-971. <https://doi.org/10.1007/s00704-019-02882-0>
- [20] Moisseeva, N. and Steyn, D.G. (2014) Dynamical Analysis of Sea-Breeze Hodograph Rotation in Sardinia. *Atmospheric Chemistry and Physics*, **14**, 13471-13481. <https://doi.org/10.5194/acp-14-13471-2014>
- [21] Simpson, J., Mansfield, D. and Milford, J. (1977) Inland Penetration of Sea-Breeze Fronts. *Quarterly Journal of the Royal Meteorological Society*, **103**, 47-76. <https://doi.org/10.1256/smsqj.43503>

- [22] Igel, A.L., van den Heever, S.C. and Johnson, J.S. (2018) Meteorological and Land Surface Properties Impacting Sea Breeze Extent and Aerosol Distribution in a Dry Environment. *Journal of Geophysical Research: Atmospheres*, **123**, 22-37. <https://doi.org/10.1002/2017jd027339>
- [23] Zhang, L., Sun, J., Ying, Z. and Xiao, X. (2021) Initiation and Development of a Squall Line Crossing Hangzhou Bay. *Journal of Geophysical Research: Atmospheres*, **126**, e2020JD032504. <https://doi.org/10.1029/2020jd032504>
- [24] Kniffka, A., Knippertz, P. and Fink, A.H. (2018) The Role of Low-Level Clouds in the West African Monsoon System. *Atmospheric Chemistry and Physics, Discussions*. <https://acp.copernicus.org/preprints/acp-2018-743/acp-2018-743.pdf>
- [25] Liang, Z. and Wang, D. (2017) Sea Breeze and Precipitation over Hainan Island: Sea Breeze and Precipitation over Hainan Island. *Quarterly Journal of the Royal Meteorological Society*, **143**, 137-151. <https://doi.org/10.1002/qj.2952>
- [26] Cautenet, S. and Rosset, R. (1989) Numerical Simulation of Sea Breezes with Vertical Wind Shear during Dry Season at Cape of Three Points, West Africa. *Monthly Weather Review*, **117**, 329-339. [https://doi.org/10.1175/1520-0493\(1989\)117<0329:nsosbw>2.0.co;2](https://doi.org/10.1175/1520-0493(1989)117<0329:nsosbw>2.0.co;2)
- [27] Laux, P., Kunstmann, H. and Bárdossy, A. (2008) Predicting the Regional Onset of the Rainy Season in West Africa. *International Journal of Climatology*, **28**, 329-342. <https://doi.org/10.1002/joc.1542>
- [28] Knippertz, P. and Fink, A.H. (2008) Dry-season Precipitation in Tropical West Africa and Its Relation to Forcing from the Extratropics. *Monthly Weather Review*, **136**, 3579-3596. <https://doi.org/10.1175/2008mwr2295.1>
- [29] Taylor, C.M., Klein, C., Parker, D.J., Gerard, F., Semeena, V.S., Barton, E.J., *et al.* (2022) “Late-Stage” Deforestation Enhances Storm Trends in Coastal West Africa. *Proceedings of the National Academy of Sciences of the United States of America*, **119**, e2109285119. <https://doi.org/10.1073/pnas.2109285119>
- [30] Crook, J., Klein, C., Folwell, S., Taylor, C.M., Parker, D.J., Bamba, A., *et al.* (2023) Effects on Early Monsoon Rainfall in West Africa Due to Recent Deforestation in a Convection-Permitting Ensemble. *Weather and Climate Dynamics*, **4**, 229-248. <https://doi.org/10.5194/wcd-4-229-2023>
- [31] Maranan, M., Fink, A.H. and Knippertz, P. (2018) Rainfall Types over Southern West Africa: Objective Identification, Climatology and Synoptic Environment. *Quarterly Journal of the Royal Meteorological Society*, **144**, 1628-1648. <https://doi.org/10.1002/qj.3345>
- [32] Dahech, S., Berges, J. and Beltrando, G. (2012) Localisation et dynamique du front de la brise de mer au Maghreb oriental. *Climatologie*, **9**, 59-81. <https://doi.org/10.4267/climatologie.189>
- [33] Lensky, I.M. and Dayan, U. (2012) Continuous Detection and Characterization of the Sea Breeze in Clear Sky Conditions Using Meteosat Second Generation. *Atmospheric Chemistry and Physics*, **12**, 6505-6513. <https://doi.org/10.5194/acp-12-6505-2012>
- [34] Ferdiansyah, M.R., Inagaki, A. and Kanda, M. (2020) Detection of Sea-Breeze Inland Penetration in the Coastal-Urban Region Using Geostationary Satellite Images. *Urban Climate*, **31**, Article ID: 100586. <https://doi.org/10.1016/j.uclim.2020.100586>
- [35] Corpetti, T. and Planchon, O. (2011) Front Detection on Satellite Images Based on Wavelet and Evidence Theory: Application to the Sea Breeze Fronts. *Remote Sensing of Environment*, **115**, 306-324. <https://doi.org/10.1016/j.rse.2010.09.003>
- [36] Corpetti, T., Planchon, O. and Dubreuil, V. (2006) Detection of the Sea Breeze Front

- from Satellite Images Using an Active Contour Method and Wavelets. 2006 *IEEE International Symposium on Geoscience and Remote Sensing*, Denver, 31 July-4 August 2006.
- [37] Kass, M., Witkin, A. and Terzopoulos, D. (1988) Snakes: Active Contour Models. *International Journal of Computer Vision*, **1**, 321-331. <https://doi.org/10.1007/bf00133570>
- [38] Cohen, L.D. (1991) On Active Contour Models and Balloons. *CVGIP: Image Understanding*, **53**, 211-218. [https://doi.org/10.1016/1049-9660\(91\)90028-n](https://doi.org/10.1016/1049-9660(91)90028-n)
- [39] Ferdiansyah, M.R. and Wijayanto, A.W. (2022) The Estimation of Sea-Breeze Front Velocity over Coastal Urban Using Himawari-8 Images: A Case Study in Jakarta. *Jurnal Meteorologi dan Geofisika*, **23**, 39. <https://doi.org/10.31172/jmg.v23i3.810>
- [40] Papolu, J.S., Bhanu Prasad, M., Vasavi, S. and Geetha, G. (2022) A Framework for Sea Breeze Front Detection from Coastal Regions of India Using Morphological Snake Algorithm. *ECS Transactions*, **107**, 585-597. <https://doi.org/10.1149/10701.0585ecst>
- [41] Guedje, F.K., Houeto, A.V.V., Houngrinou, E.B., Fink, A.H. and Knippertz, P. (2019) Climatology of Coastal Wind Regimes in Benin. *Meteorologische Zeitschrift*, **28**, 23-39. <https://doi.org/10.1127/metz/2019/0930>
- [42] Tozer, B., Sandwell, D.T., Smith, W.H.F., Olson, C., Beale, J.R. and Wessel, P. (2019) Global Bathymetry and Topography at 15 Arc Sec: SRTM15+. *Earth and Space Science*, **6**, 1847-1864. <https://doi.org/10.1029/2019ea000658>
- [43] Henken, C.C., Schmeits, M.J., Deneke, H. and Roebeling, R.A. (2011) Using MSG-SEVIRI Cloud Physical Properties and Weather Radar Observations for the Detection of Cb/TCu Clouds. *Journal of Applied Meteorology and Climatology*, **50**, 1587-1600. <https://doi.org/10.1175/2011jamc2601.1>
- [44] Damato, F., Planchon, O. and Dubreuil, V. (2003) A Remote-Sensing Study of the Inland Penetration of Sea-breeze Fronts from the English Channel. *Weather*, **58**, 219-226. <https://doi.org/10.1256/wea.50.02>
- [45] Chan, T.F. and Vese, L.A. (2001) Active Contours without Edges. *IEEE Transactions on Image Processing*, **10**, 266-277. <https://doi.org/10.1109/83.902291>
- [46] Marquez-Neila, P., Baumela, L. and Alvarez, L. (2014) A Morphological Approach to Curvature-Based Evolution of Curves and Surfaces. *IEEE Transactions on Pattern Analysis and Machine Intelligence*, **36**, 2-17. <https://doi.org/10.1109/tpami.2013.106>
- [47] Osher, S. and Sethian, J.A. (1988) Fronts Propagating with Curvature-Dependent Speed: Algorithms Based on Hamilton-Jacobi Formulations. *Journal of Computational Physics*, **79**, 12-49. [https://doi.org/10.1016/0021-9991\(88\)90002-2](https://doi.org/10.1016/0021-9991(88)90002-2)
- [48] Getreuer, P. (2012) Chan-Vese Segmentation. *Image Processing On Line*, **2**, 214-224. <https://doi.org/10.5201/ipol.2012.g-cv>
- [49] Alvarez, L., Baumela, L., Márquez-Neila, P. and Henríquez, P. (2012) A Real Time Morphological Snakes Algorithm. *Image Processing On Line*, **2**, 1-7. <https://doi.org/10.5201/ipol.2012.abmh-rtmsa>
- [50] Gajewicz-Skretna, A., Kar, S., Piotrowska, M. and Leszczynski, J. (2021) The Kernel-Weighted Local Polynomial Regression (KwLPR) Approach: An Efficient, Novel Tool for Development of QSAR/QSAAR Toxicity Extrapolation Models. *Journal of Cheminformatics*, **13**, Article No. 9. <https://doi.org/10.1186/s13321-021-00484-5>

## Appendix A. Implementation of the Morphological Snake Algorithm

Monotonic contrast and translation invariant operators are called morphological operators. The most common are the dilation and erosion operators.

A  $D_h$  dilatation of  $h$  of the function  $u$  is defined as follows:

$$D_h u(x) = \sup_{y \in hB(0,1)} u(x+y) \quad (\text{A1})$$

and an  $E_h$  Erosion defined by:

$$E_h u(x) = \inf_{y \in hB(0,1)} u(x+y) \quad (\text{A2})$$

In both definitions,  $B(0,1)$  is the ball of radius 1 centered on 0 and the  $hB$  term is the set  $B$  scaled by  $h$ , i.e.,  $hB = \{h_x : x \in B\}$ .

An interesting result in mathematical morphology is that each T morphological operator admits a sup-inf representation in the form:

$$T_h u(x) = \sup \inf_{B \in \mathcal{B}_y \in x+hB} u(x) \quad (\text{A3})$$

Or a double representation inf-sup

$$T_h u(x) = \inf \sup_{B \in \mathcal{B}_y \in x+hB} u(x) \quad (\text{A4})$$

In both cases,  $T$  is a set of structuring elements that uniquely defines the operator, and  $h$  is the size of the operator  $B$ . For example, by choosing an eigenbasis, one can express dilatations and erosions in a form sup-inf or inf-sup. The dilation of radius  $h$  admits an inf-sup form when  $B$  consists of the unique structuring element,  $\{B(0,1)\}$ . Also, erosion admits a sup-inf shape using the same basis.

Finally, the composition order of  $SI_d$  and  $IS_d$  operators could be either  $SI_d \circ IS_d$  or  $IS_d \circ SI_d$  since the addition is commutative. Here we have chosen the first order. However, in practice, to balance the contribution  $SI_d$  of the two choices of operator composition, we alternate them by iterations. The operator  $SI_d \circ IS_d$  is calculated in two steps: first,  $IS_d$  step, which in 2D is:

$$u^{n+1}(x) = \min_{P \in B(\nabla_i, \nabla_j) \in B} \max_{P \in B(\nabla_i, \nabla_j) \in B} u^n(i + \nabla_i, j + \nabla_j) \quad (\text{A5})$$

And then the  $SI_d$  step in 2D is:

$$u^{n+1}(x) = \max_{P \in B(\nabla_i, \nabla_j) \in B} \min_{P \in B(\nabla_i, \nabla_j) \in B} u^n(i + \nabla_i, j + \nabla_j) \quad (\text{A6})$$

Finally, the successive application of the morphological curvature operator  $SI_d \circ IS_d$ , of  $B^2$  basic is equivalent to the solution of PDE (Equation (4)) and (Equation (5)).

Since we now have a group of basic morphological tools (Dilation, Erosion and Curvature) that act like FDEs (Equation (4)) and (Equation (5)), which are essential for various computer vision applications, and contour evolution, we can combine these tools to obtain an approximate solution (i.e. use mathematical morphology to improve contours).

Let  $u : \Omega \subset N^2 \rightarrow R$

$(x, y) \rightarrow u(x, y)$  A Levels-set function set on a domain  $\Omega$  of an image.

The fronts, noted  $C$  are represented by the zero Level-set defined implicitly via a function of Lipschitz by

$$C(t) = \{(x, y); u(t, (x, y)) = 0\}$$

and the evolution of the curve is given by the zero-level curve at the time  $t$  of the function  $u(t, x, y)$ .

Making the curve evolve in the normal direction with the speed amounts to solving the differential equation: Osher and Sethian [47]

$$\frac{\partial u}{\partial t} = F \cdot |\nabla u|, \quad u(t, x, y) = u_0(x, y) \tag{A7}$$

where the set  $\{(x, y); u_0(x, y) = 0\}$  defines the initial contour.

A special case is motion by mean curvature when

$$F = \operatorname{div} \left( \frac{\nabla u}{|\nabla u|} \right) \text{ is the curvature of the contour line passing through } u(x, y).$$

The equation thus becomes:

$$\begin{cases} \frac{\partial u}{\partial t} = \operatorname{div} \left( \frac{\nabla u}{|\nabla u|} \right) \cdot |\nabla u|, & t \in (0, \infty), \quad x \in \mathbb{R}^2 \\ u(t, x, y) = u_0(x, y), & x \in \mathbb{R}^2 \end{cases} \tag{A8}$$

Let us apply this idea to solve the FDE contour evolution ACWE (Equation (5)) and GAC (Equation (4)). For the implementation we choose the first one (*i.e.*, ACWE). The  $SI_d \circ IS_d$  operator approximates the smoothing term, erosion and dilation approximate the curvature. The term image attraction is new, but it is not difficult to derive its morphological approximation.

When  $\lambda_1 |\nabla u| (I - C_1)^2 < \lambda_2 |\nabla u| (I - C_2)^2$  at  $X$ ,  $X$  belongs to the interior of the curve; if the inequality is reversed, belongs to the outside of the curve; if not, stay where it was.

As before, the hypersurface should be defined as the set of levels of a binary integration function.

$$u : Z^d \rightarrow \{0, 1\}$$

The ACWE morphological algorithm is given by the following three steps:

$$u^{n+\frac{1}{3}}(x) = \begin{cases} (Du^n)(x), & \text{if } v > 0 \\ (Eu^n)(x), & \text{if } v < 0 \\ u^n(x), & \text{Moreover} \end{cases}$$

The ACWE morphological algorithm is given by the following three steps:

$$u^{n+\frac{2}{3}}(x) = \begin{cases} 1, & \text{if } \left| \nabla u^{n+\frac{1}{3}} \right| \left( \lambda_1 (I - C_1)^2 - \lambda_2 (I - C_2)^2 \right) (x) < 0 \\ 0, & \text{if } \left| \nabla u^{n+\frac{1}{3}} \right| \left( \lambda_1 (I - C_1)^2 - \lambda_2 (I - C_2)^2 \right) (x) > 0 \\ u^{n+\frac{1}{3}}, & \text{Furthermore} \end{cases}$$

$$u^{n+1}(x) = \left( (SI \circ IS)^u u^{\frac{n+2}{3}} \right)(x) \tag{A9}$$

We use a numerical method to solve the gradient equation (or a system of equations) to find this boundary. The method uses operations such as morphological operations and gradient calculations to update the segmentation boundary.

### Appendix B. Numerical Scheme for ACWE

To obtain the global minimum of the functional energy, we first define the regularization of the Heaviside and Dirac functions. These functions are defined by:

$$H_\varepsilon(x) = \frac{1}{2} \left( 1 + \frac{1}{\pi} \arctan \left( \frac{x}{\varepsilon} \right) \right) \quad \text{and} \quad \delta_\varepsilon(x) = \frac{1}{\pi} \frac{\varepsilon}{\varepsilon^2 + x^2} \tag{B1}$$

where  $H_\varepsilon(x)$ : is the Heaviside function and  $\delta_\varepsilon(x)$  the Dirac function

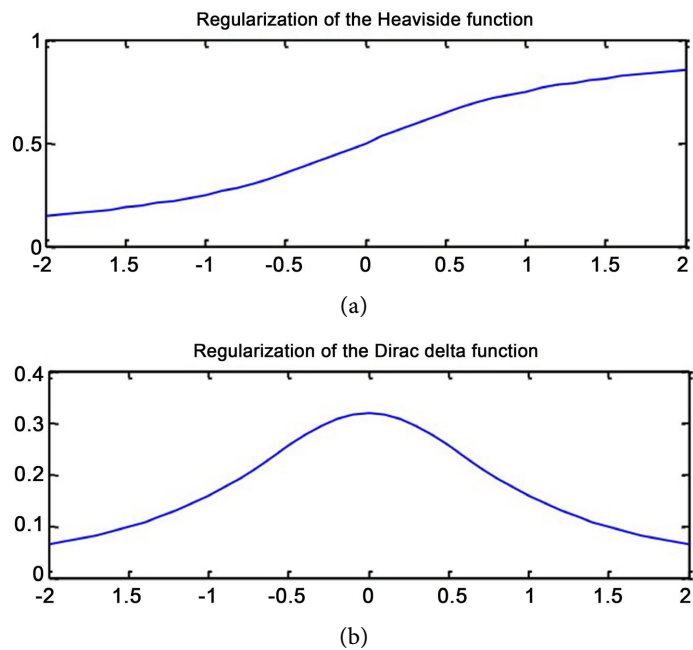


**Figure A1.** Regularization function. (Rami Cohen, 2010).

The integrator function  $u$  is stored in d-dimensional array with Boolean (binary basis) values in each cell. The dilation at each cell is implemented as the maximum of the values of  $u$  in the neighborhood of the cell. Similarly, the erosion is the minimum of the values of  $u$  in the vicinity of the cell. The neighborhood is defined as the Moore neighborhood (around the central cell), *i.e.* the set of cells at a Chebyshev distance of 1. For example, in the 2D case, the Dilation is:

$$u_{n+1}(i, j) = \max_{\nabla_i, \nabla_j \in \{-1, 0, 1\}} u^n(i + \nabla_i, j + \nabla_j) \tag{B2}$$

And the Erosion

$$u_{n+1}(i, j) = \min_{\nabla_i, \nabla_j \in \{-1, 0, 1\}} u^n(i + \nabla_i, j + \nabla_j) \tag{B3}$$

The gradient is the  $d$ -dimensional vector consisting of all the directional derivatives,  $\nabla_u = [u_x, u_y, \dots]$ . Derivatives are calculated using central differences. For example, in 2D, the derivatives of  $u$  with respect to  $x$  and  $y$  are calculated as follows:

$$u_x(i, j) = \frac{1}{2}(u(i+1, j) - u(i-1, j)) \quad (\text{B4})$$

$$u_y(i, j) = \frac{1}{2}(u(i, j+1) - u(i, j-1)) \quad (\text{B5})$$

The parameters of the Active Contour Without Edge (ACWE) model are much easier to define and less sensitive to disturbances than those of the Geodesic Active Contour (GAC) model. Balloon power is rarely needed. It works directly on the image. It does not use a  $g$ -stop criterion. For our application, we set  $\varepsilon = \lambda_1 = \lambda_2 = 1$  and  $\nu = 0$ . The regularisation force should be small when searching for small features and large otherwise.